Word Count 10524

(Revision 2) Experimental investigation of trace element partitioning between amphibole and alkali basaltic melt: towards a more general partitioning model with implications for amphibole fractionation at deep crustal levels

Barbara Bonechi[1,2*], Alessandro Fabbrizio[3], Cristina Perinelli[1,4], Mario Gaeta[1], Maurizio Petrelli[5]

[1]Dipartimento di Scienze della Terra, Sapienza Università di Roma, P.le Aldo Moro 5, 00185, Rome, Italy

[2]Department of Earth and Environmental Sciences, University of Manchester, Williamson Building, Oxford Road, Manchester M13 9PL

[3]Institute of Petrology and Structural Geology, Faculty of Science, Charles University, Albertov 6, 12843 Prague, Czech Republic

[4]Consiglio Nazionale delle Ricerche, Istituto di Geologia Ambientale e Geoingegneria, Sede Secondaria di Roma, c/o Dipartimento di Scienze della Terra, Sapienza Università di Roma, P.le A. Moro 5, Rome, Italy

[5]Department of Physics and Geology, University of Perugia, Piazza Università, Perugia 06100, Italy

*E-mail corresponding author: barbara.bonechi@uniroma1.it, barbara.bonechi@manchester.ac.uk

ABSTRACT

Time-series experiments were carried out in a piston cylinder apparatus conducted at 0.8 GPa and 1030-1080 °C using as starting material a hydrous K-basalt melt to determine the element partition coefficients between amphibole and silicate glass. Major, minor, and trace element compositions of

amphibole and glass were determined with a combination of electron microprobe and laser ablation inductively coupled plasma mass spectrometry. Results show that the main mineral phase is calcic amphibole, and the coexisting glass compositions range from basaltic trachyandesite to andesite. We estimated the ideal radius, the maximum partition coefficient and the apparent Young's modulus of the A, M1-M2-M3, and M4-M4' sites of amphibole. The influence of melt and amphibole composition, temperature, and pressure on the partition coefficients between amphiboles and glasses has also been investigated by comparing our data with a literature dataset spanning a wide range of pressures (0.6-2.5 GPa), temperatures (780-1100 °C), and compositions (from basanite to rhyolite). Finally, we modelled a deep fractional crystallization process using the amphibole-melt partition coefficients determined in this study, observing that significant amounts of amphibole crystallization (>30 wt%) well reproduce the composition of an andesitic melt similar to that of the calcalkaline volcanic products found in Parete and Castelvolturno bore-holes (NW of Campi Flegrei, Italy).

Keywords: amphibole; trace element partition coefficient; lattice strain model; Campi Flegrei

INTRODUCTION

The occurrence of amphibole in rocks encompassing the entire range of silica activities in terrestrial igneous suites, coupled with its capacity to incorporate significant concentrations of geochemically important trace elements, underscores the likely importance of this phase in the chemical evolution of both mantle- and crustal-derived magmas (Brenan et al. 1995; Tiepolo et al. 2007). During the last decades, the behavior of trace element partitioning between calcic amphiboles and silicate melts has been investigated at different pressures (0.2-2.7 GPa), temperatures (750-1150 °C), and system compositions (e.g., Nicholls and Harris 1980; Adam et al. 1993; Adam and Green 1994, 2003; Sisson 1994; LaTourrette et al. 1995; Brenan et al. 1995, 1998; Klein et al. 1997; Tiepolo et al. 1999, 2000a,

2020b, 2007; Hilyard et al. 2000a; Zhang et al. 2019). It is widely accepted that the resulting partition coefficients depend on the chemical compositions of mineral and melt phases, pressure, temperature, and H_2O-content of the melt, as well as on the redox conditions (Blundy and Wood 2003; Adam and Green 2006; Aigner-Torres et al. 2007; Severs et al. 2009; van Kan Parker et al. 2010; Hill et al. 2011; Fabbrizio et al. 2021). Moreover, Blundy and Wood (1994) provided a theoretical framework based on the lattice strain model (Brice 1975) for the interpretation of trace element partitioning. So far, it has been applied successfully to trace element partitioning between pyroxene (e.g., Wood and Blundy 1997; Schmidt et al. 1999; Adam and Green 2006; Sun and Liang 2012, 2013; Mollo et al. 2018; Bonechi et al. 2021; Fabbrizio et al. 2021), olivine (e.g., Zanetti et al. 2004; Sun and Liang 2013), garnet (e.g., Draper and van Westrenen 2007; van Westrenen and Draper 2007; Sun and Liang 2013), amphibole (e.g., LaTourrette et al. 1995; Adam and Green 2006; Tiepolo et al. 2007; Wan et al. 2009; Nandedkar et al. 2016; Shimizu et al. 2017; Zhang et al. 2019; Cannaò et al. 2022), phlogopite (e.g., LaTourrette et al. 1995; Schmidt et al. 1999; Fabbrizio et al. 2010), leucite (e.g., Schmidt et al. 1999; Fabbrizio et al. 2008), feldspars (e.g., Icenhower and London 1996; Fabbrizio et al. 2009) and their coexisting melts. Despite numerous investigations on the partition between crystals and melt, there are still some mineral phases, including amphibole, for which data are limited or missing. In this study we provide new data on amphibole major, minor, and trace elements partition coefficients derived from crystallization experiments on a hydrous K-basaltic melt at 0.8 GPa and 1030-1080 °C. In detail, we analysed major and trace elements in amphiboles and glasses of the experimental runs by using an electron microprobe and laser ablation-inductively coupled plasma-mass spectrometry, respectively. We determined the concentrations of large ion lithophile elements, rare earth elements, high field strength elements, and transition metals in experimental phases and then, we used the obtained data to calculate the partition coefficients between amphiboles and glasses. In addition, we estimated the ideal radius, the maximum partition coefficient, and the apparent Young's modulus of the A, M1-M2-M3,

and M4-M4' sites of amphibole. Also, we reviewed the influence of melt and amphibole compositions, temperature, and pressure on the behavior of partition coefficients between amphiboles and glasses by integrating our data with a literature data set (LEPR database and data from Nandedkar et al. 2016, Zhang et al. 2019, and Cannaò et al. 2022) spanning a wide range of pressures (0.6-2.5 GPa), temperatures (780-1100 °C) and compositions (from basanite to rhyolite). Finally, we observed whether a composition approaching the APR16 one is able, through the crystallization of amphibole in a deep differentiation process, to produce an andesite melt with trace element abundances similar to those of the calc-alkaline volcanic products found in Parete and Castelvolturno bore-holes (NW of Campi Flegrei, Italy).

METHODS

Samples' description

Crystallization experiments were performed by using the end loaded piston cylinder apparatus at the HP-HT Laboratory of the Earth Sciences Department (Sapienza University, Rome, Italy). Experiments were carried out at isobaric conditions of 0.8 GPa, 1030-1080 °C, with an initial H_2O content ≥3 wt%, and durations from 0.25 to 9 hours. Experiments were performed at different duration to observe the variation of trace elements concentration with time in both disequilibrium and equilibrium conditions. We used as starting materials the powder of a natural primitive K-basalt (APR16) and its glass (APR16GL, Table 1), prepared by melting the APR16 powder in a Fe-saturated Pt container for 15 min using a CO/CO_2 gas mixing furnace installed at the Bayerisches Geoinstitut (Bayreuth, Germany) at 1400 °C, atmospheric pressure and oxygen fugacity corresponding to the NNO (nickel-nickel oxide) buffer. The as-fused starting material did not contain crystalline phases, as analysed by both microprobe and SEM image analyses. Then, the obtained glassy starting material was ground in an agate mortar under acetone. The natural primitive K-basalt (APR16 sample) was found as scoria clast

in the deposits of the Solchiaro hydromagmatic eruption (~22 ka ago; Morabito et al. 2014) located in Procida Island (Campi Flegrei, Italy). This K-basalt is characterized by 12 vol% of forsteritic olivine and diopsidic clinopyroxene phenocrysts dispersed in a groundmass made of olivine, clinopyroxene, plagioclase, Ti-magnetite, alkali feldspar, and glass (D'Antonio et al. 1999; De Astis et al. 2004). Although amphibole is not present in outcropped products, its stability has been experimentally observed when using APR16 as a starting composition, equilibrated at P = 0.8 GPa when water contents are > 7 wt.% (Bonechi et al. 2017; Perinelli et al. 2019; Bonechi et al. 2020a, 2020b).

Experimental techniques

The detailed experimental procedure is described by Perinelli et al. (2019) and by Bonechi et al. (2020a, 2020b). Here we report the main aspects. Assemblies were 1.25 cm in diameter, and consisted of CaF_2 outer sleeve, graphite furnace, and crushable magnesia spacers were used.

The experimental charges were prepared loading $Au_{75}Pd_{25}$ capsules with ~40 mg of sample powder. In each experiments, we added water in known amounts by using a 1.0 μL microsyringe (Table 2). Loss of H_2O by vaporization during welding was prevented by freezing the crucible with nitrogen. The welded capsule was weighed, stored in a furnace at 110 °C for at least 1 h, and then weighed again to confirm the absence of water leaks. Moreover, to minimize possible loss of H_2 during the experiments the charges were surrounded by pyrophyllite powder (Freda et al. 2001). The temperature was controlled by a factory-calibrated W_3Re_{97}-$W_{25}Re_{75}$ (type D) thermocouple and maintained with an uncertainty of ± 5 °C. For the experimental run-up, we used the "hot piston-out" procedure (Johannes et al. 1971; Presnall et al. 1978) in which the assembly was first cold-pressurized to a value ~10% over the target pressure and then heated to the final run temperature. This technique allows to closely approach the run pressure through the stress relaxation within the assembly upon heating, requiring only minor upward pressure adjustments during the experiment in most cases (Watson et al. 2002). The

heating rate was imposed at 150 °C/min. The samples were maintained at the target pressure and temperature for a given duration (nominal duration; Table 2), and then quenched by turning off the power. The temperature drop below 500 °C was of <5 s (average cooling rate of 150 °C/s). All the runs were self-buffered; an estimation of experimental fO_2 was made by using the theoretical model of Barr and Grove (2010), which is based on the temperature-and fO_2-dependent partitioning of Fe between the AuPd capsule and coexisting melt. Thus, we measured the post-run Fe content in the sample-holder as closely as possible to the capsule-sample boundary of a near-liquidus anhydrous experiment. Applying the Barr and Grove (2010) approach the calculated fO_2 were of NNO -0.5 for the near-liquidus run and NNO -0.8 and NNO -1.1 for the longest runs of this study (Bonechi et al. 2020a). As a whole, the estimated range of fO_2 values agree with those estimated for similar furnace assemblages (Conte et al. 2009; Weaver et al. 2013; Perinelli et al. 2019; Bonechi et al. 2020a). Finally, we determined the undercooling (ΔT; Table 2) that is the difference between the liquidus temperature and the nominal temperature of the experiment (Bonechi et al. 2020a, 2020b; Bonechi 2020). For calculations, the liquidus temperature (T_L) of APR16 experiments was taken from Procida K-basalt experimental data (1095 °C; Perinelli et al. 2019, Bonechi et al. 2020a).

Analytical techniques

Textural investigations and major element determinations. Back-scattered electron (BSE) images used to investigate textural aspects of both natural and experimental samples were collected by Scanning Electron Microscopy using a FEI-quanta 400 equipped for microanalysis with an EDAX Genesis system at the Earth Sciences Department, Sapienza University of Rome. Major elements were analysed at the CNR-Istituto di Geologia Ambientale e Geoingegneria di Roma, with a Cameca SX50 electron microprobe equipped with five wavelength dispersive spectrometers. Quantitative analyses were performed using 15 kV accelerating voltage and 15 nA beam current. As standards we employed

metals for Mn and Cr, Jadeite for Na, Wollastonite for Si and Ca, Orthoclase for K, Corundum for Al, Magnetite for Fe, Rutile for Ti, Periclase for Mg, Apatite for P. Counting times for all elements were 20 s on peak and 10 s on both backgrounds. Light elements (Na, K) were counted first to prevent loss by volatilization. The PAP correction method was used. Minerals were analysed using a beam diameter of 1 μm whereas to minimize alkali loss during glass analysis, the beam was defocused to 15 μm. To evaluate the accuracy of the analyses, repeated analyses of three international secondary standards (Kakanui augite, Icelandic Bir-1, and rhyolite RLS132 glasses from USGS) were made before any series of measurements. The mean precision from the standard value was about 1% for SiO_2, 2% for Al_2O_3, 5% for K_2O, CaO and FeO, and 8-10% for other elements. The analytical precision (2 sigma error) is ≤1% for elements in the concentration range >10 wt% oxide, 5% for elements in the range 2–10 wt% oxide, and better than 10% for elements in the range 0.5-2 wt% oxide. The water contents of experimental glasses were estimated according to the by-difference method (Devine et al. 1995; Humphreys et al. 2006). We are aware that this method is not fully reliable given the estimation is affected by *i*) element concentrations not measured by EMPA and *ii*) surface charge effects (Hughes et al. 2019) leading to an overestimation of H_2O concentration. However, the obtained H_2O values show a good linear correlation (correlation coefficient $R^2 = 0.97$) with those determined by micro-Raman spectroscopy measurements on residual melts of equilibrium experiments performed on the same composition, at the same P, T, and initial hydrous conditions (cf. Perinelli et al. 2019).

Laser ablation-inductively coupled plasma mass spectrometry (LA-ICP-MS). LA-ICP-MS analyses of the experimental samples were performed at the Department of Physics and Geology, University of Perugia (Italy). The instrumentation consisted of a Teledyne/Photon Machine G2 LA device equipped with a Two-Volume ANU HelEx 2 cell and coupled with a Thermo Fisher Scientific quadrupole-based iCAP-Q ICP-MS. The analyses of amphibole crystals and glasses were performed

using a circular laser beam of 12-20 μm diameter, a frequency of 10-15 Hz and a laser density on the sample surface of 3.5 J/cm^2. Oxide formations was checked on the NIST SRM 612 by monitoring and maintaining the ratio ThO/Th ratio below 0.005. The NIST SRM-610 standard reference material was used as calibrant and Ca, previously analysed by EPMA, as internal standard. Under these operating conditions precision and accuracy are better than 10% for most of the elements (Petrelli et al. 2007, 2008, 2016). In detail, at beam sizes equal or larger than 15 μm, precision (measured as one sigma) and accuracy (expressed as relative deviation from the reference value) are of the order of 10% (Petrelli et al. 2016). Accuracy is better or equal to 10% and 13% at beam sizes of 15 and 10 μm, respectively, while when the spatial resolution is increased to 12 μm, accuracy remains better than 15% (Petrelli et al. 2016).

RESULTS

Texture, phase relationships and chemical composition of experimental samples

All the experimental samples investigated in this study, except the APR16-ST1 run, are described in detail in the previous work of Bonechi et al. (2020a) dealing with phase equilibria and crystallization kinetics in the APR16 K-basalt. Here we briefly report a description of the main aspects.

Texture and phase relationships. All the experimental products that for simplicity we have grouped into the C3A (i.e., C3Aa, C3Ab, C3Ad runs) and C3B (C3Ba, C3Bb, C3Bc, C3Bd runs) suites, show a high crystallinity (Fig. 1a, b and Table 2) as a consequence of the imposed undercooling (ΔT = 150-200 °C), that yields strong supersaturation conditions in the K-basaltic melt, enhances the nucleation kinetics in the sample during the early stage of experiments, and affects the phase modal proportions (Bonechi et al., 2020a and reference therein). Amphibole (Amph) occurs in all the experiments as euhedral crystals of ~40 μm in size, along with clinopyroxene (Cpx) + oxide (Ox) ± plagioclase (Plg) ± orthopyroxene (Opx) (Table 2). Both tiny crystals of Cpx and Opx (up to ~5 μm sized) are euhedral in

193 shape, as the larger (~40 μm in size) Ox grains. Subhedral to euhedral plagioclase has dimensions of
194 about 10 μm or less (Bonechi et al. 2020a). Glass is present in all the experimental runs, but it was
195 analysed only in those with glass portions large enough to be examined.
196 About the APR16-ST1 experiment (Fig. 1c and Table 2), it is similar to the two runs with the longest
197 duration, i.e., C3Ad and C3Bd, in both texture and mineral assemblage. It is formed by abundant Amph
198 showing well-developed crystal face and dimensions up to ~50 μm, combined with idiomorphic Cpx of
199 ~5 μm in size and euhedral Ox (sized up to ~40 μm). Glass pools larger than 60 μm occur within all the
200 capsule. It is also characterized by large (up to 100 μm) and numerous vesicles present throughout the
201 sample as a result of the high amount of water added before the experiment (H_2O_i = 8 wt%), which
202 favored the achievement of saturation conditions (APR16 H_2O solubility ~10 wt%; Perinelli et al.
203 2019).
204 *Chemical composition.* Chemical compositions of Amph are reported in Table S1 of Supplementary
205 Material 2. According to the Hawthorne et al. (2012) classification, all the crystallized Amph is calcic,
206 and its composition varies from magnesiohorneblende and edenite to pargasite and
207 magnesiohastingsite. Cpx compositions are diopsidic ($Wo_{46-48}En_{39-43}Fs_{10-14}$), whereas the
208 orthopyroxene crystals found in the APR16-C3Bc run is enstatitic ($Wo_4En_{73}Fs_{23}$). Oxide crystals are
209 generally hercynites, while in the APR16-C3Aa run Cr-rich spinels also occur. Plagioclase grains
210 occurring in the shortest runs (0.25-3 h) are bytownitic (An_{72}) and labradoritic (An_{62}) in composition.
211 As regards Amph, the calculated Amph-melt Fe-Mg exchange coefficient (i.e., $^{Amph\text{-}liq}K_{DFe\text{-}Mg}$ =
212 $(FeO/MgO)^{Amph}/(FeO/MgO)^{liq}$) for the runs of the C3A and C3B suites varies between ~0.3 and ~1,
213 showing an almost linear decrease with increasing time (Bonechi et al. 2020a) and a non-achievement
214 of equilibrium conditions in many of the experiments. Indeed, only the magnesiohastingsites
215 crystallized in the runs at 9 h (i.e., APR16-C3Ad and APR16-C3Bd with $^{Amph\text{-}liq}K_{DFe\text{-}Mg}$ = 0.34 and
216 0.40, respectively) attained Amph-liquid equilibrium conditions ($^{Amph\text{-}liq}K_{DFe\text{-}Mg}$ = 0.28 ± 0.11; Putirka

2016). In addition to these, also the magnesiohastingsite crystallized in the run APR16-ST1, carried out for 2 h in saturation conditions (H_2O_i = 8 wt.%; Table 2), achieved Amph-liquid equilibrium conditions ($^{Amph\text{-}liq}K_{DFe\text{-}Mg}$ = 0.32). As regards the other phases, instead, Cpx and Plg result to be always in disequilibrium conditions. Chemical compositions of synthetic glasses, that according to TAS diagram (Le Bas et al. 1986) range from basaltic trachy-andesite to andesite (Fig. S1 of Supplementary Material 1), are reported in Table S2 of Supplementary Material 2.

Trace and REE content

Average compositions of trace elements concentrations analysed by LA-ICP-MS technique in Amph, and coexisting glass are reported in Table 3.

Amphibole. Figure 2 shows the trace elements concentrations in Amph normalized to chondrite C1 after Anders and Grevesse (1989) for LILEs (Large-Ion Lithophile Elements), REEs (Rare Earth Elements), HFSEs (High Field Strength Elements), and TEs (Transition Elements). The abundance of LIL elements (e.g., Rb and Ba) of Amph from all experiments are comparable among them except for Pb which shows significant differences in its content. The chondrite-normalized REE patterns display enrichment of light REE (LREE) over heavy REE (HREE) (i.e., La_N/Yb_N = 3.5-6.2, where the subscript *N* denotes chondrite-normalized values) with a maximum at La_N (~74). All Amph exhibit no Eu anomaly (Eu/Eu* = 0.98-1.06; Eu/Eu* = $Eu_N/(Sm_N \times Gd_N)^{1/2}$) indicating the absence or scarce crystallization of coexisting plagioclase. Finally, the concentration of tetravalent HFSEs (i.e., Hf, Zr, Ti) is lower than that of pentavalent cations (i.e., Ta and Nb), while as regards TEs, it is possible to see evident troughs at Co and Ni compared to the nearby elements.

Glass. Figure 3 shows the trace elements concentration in the experimental glasses normalized to chondrite C1 after Anders and Grevesse (1989) for LILEs, REEs, HFSEs, and TEs. Generally, all the

experimental glasses match the trend of the APR16 sample (Mazzeo et al. 2014) and of the APR16 suite of Bonechi et al. (2021), except for Ni abundances, which are relatively higher. C1-normalized trace element patterns are L-MREE (Light/Middle rare earth element) enriched (La_N = 105-128, La_N/Sm_N = 3.0-4.6, La_N/Yb_N = 5.6-9.5) and nearly flat in the HREE region (Ho_N/Yb_N = 0.7-1.1). All the considered glasses have absent or slightly positive Eu anomaly (Eu/Eu* = 1.01-1.11). Moreover, pentavalent HFSEs (i.e., Ta and Nb) are more abundant than tetravalent cations (i.e., Zr, Hf, Ti).

DISCUSSION

Partition coefficients

Table 4 reports the trace elements Amphibole-melt *D*-values obtained in the present study for the longest experiments of the C3A and C3B suites and for APR16-ST1 run, where amphiboles are in equilibrium with the melt. Unfortunately, due to the impossibility to obtain reliable trace element concentrations of the glasses in the runs with shorter duration and in disequilibrium, we could not quantitively compare the partition coefficients in both disequilibrium and equilibrium conditions. However, the trace element concentrations measured in Amph do not show significant variation except a slight decrease or increase in the ones at equilibrium conditions (i.e., APR16-C3Ad, APR16-C3Bd, APR16-ST1; Table 3 and Fig. S2 of Supplementary Material 1). Qualitatively, this seems to suggest higher Amph-melt *D*-values for incompatible elements (e.g., LILE, REE, HFSE) and lower Amph-melt *D*-values for compatible elements (e.g., TE) in disequilibrium conditions, due to an excessive accumulation or depletion of trace elements, depending on their degree of compatibility or incompatibility, at the crystal-melt interface with a consequent disequilibrium element uptake during crystal growth (Bonechi et al. 2021 and reference therein). Figure 4 shows the partition coefficients between amphibole and melt for LILEs, REEs, HFSEs, and TEs. LILEs are incompatible (e.g., D_{Sr}

≤0.6, D_{Ba} ≤0.5). Noteworthy is the beahviour of lithium that, in agreement with literature data (e.g., D_{Li} = 0.3 in Dostal et al. 1983), results in incompatible behavior in the APR16-ST1 amphiboles but becomes almost compatible in crystals from the APR16-C3Ad (D_{Li} = 0.84) and APR16-C3Bd (D_{Li} = 0.75) runs (Table 4). This contrasting beahviour may have been induced by the different initial H_2O content (H_2O_i) between the APR16-C3Ad/Bd (H_2O_i = 3-4 wt%) and APR16-ST1 (H_2O_i = 8 wt%) experiments, which influenced the kinetic of Amph growth. Indeed, although the ΔT, that is one of the parameters controlling the crystal growth regime, is high for all experiments (Table 2), the H_2O-saturated condition of APR16-ST1 run (ΔT = 100 °C) still allowed for slow Amph growth and selectivity in elements partitioning from the beginning of the experiment, whereas H_2O-undersaturated condition of APR16-C3Ad/Bd experiments (ΔT = ~140-200 °C) probably promoted an initial rapid, disequilibrium growth of Amph and less selectivity in elements partitioning. The experimental duration of APR16-C3Ad/Bd experiments (9 h), may not have been enough for the diffusive re-equilibration of some elements such as lithium, whose abundance in APR16-C3Ad/Bd runs is always higher than in APR16-ST1 one (Table 3). LREEs (e.g., D_{La} ≤0.4) are always more incompatible than MREE and HREEs, which in some cases result to be compatible with Amph (e.g., D_{Tb} in all the considered runs, D_{Sm} to D_{Tm} in APR16-C3Bd, and D_{Sm}, D_{Er} in APR16-ST1). As regards HFSEs, tetravalent and pentavalent-charged cations are always incompatible (D_{Nb} and D_{Ta} ≤0.7; D_{Zr} and D_{Hf} between 0.5 and 0.8), with the exception of Ti. Finally, trace element partition coefficients of TEs (i.e., D_{Co}, D_{Cr}, D_{Ni}, D_{Sc}, and D_V) range from slightly incompatible to highly compatible. In particular, D_V vary between 0.7 and 1.3, whereas D_{Co}, D_{Sc}, D_{Ni}, and D_{Cr} are between 2 and 9.

Lattice strain model (LSM)

At equilibrium, the amph/melt partition coefficient can be quantitatively described by the near-parabolic relationship (Brice 1975; Blundy and Wood 1994; Wood and Blundy 2001):

This is the peer-reviewed, final accepted version for American Mineralogist, published by the Mineralogical Society of America.
The published version is subject to change. Cite as Authors (Year) Title. American Mineralogist, in press.
DOI: https://doi.org/10.2138/am-2022-8536. http://www.minsocam.org/

289

290 $$D_j^{crystal-melt} = D_0 exp\left[\frac{-4\pi E N_A}{RT}\left(\frac{r_0}{2}\left(r_j - r_0\right)^2 - \frac{1}{3}\left(r_0 - r_j\right)^3\right)\right] \quad (1),$$

291

292 where D_0 is the amphibole-melt partition coefficient for the strain-free substitution; r_0 is the optimum
293 radius for the lattice site; r_j is the ionic radius of the element of interest in the appropriate co-ordination
294 taken from Shannon (1976); E is the apparent Young's modulus for the lattice site (GPa); R is the gas
295 constant (8.3144 $J \cdot mol^{-1} \cdot K^{-1}$); N_A is Avogadro constant and T is the temperature in K. The apparent
296 Young's modulus E controls the tightness of the parabola, and D_0 determines the apex of the parabola
297 with corresponding ideal lattice site r_0.
298 To apply the lattice strain model (LSM) and fit the experimentally determined trace element partition
299 coefficients, we used the SIMPLE FIT program (Dalou et al. 2018), a lattice strain model fit by a
300 differential-evolution-constrained algorithm (Storn and Price 1997) adapted to be error weighted. In
301 presence of a small number of measured trace elements, the program failed to produce good fits.
302 Therefore, following Dalou et al. (2018), we reduced the parameter space from the default range (D_0
303 min and/or D_0 max; E min and/or E max; r_0 min and/or r_0 max) to overcome this limitation. Best-fit
304 parabolas determined for monovalent, divalent, trivalent, and tetravalent cations are plotted in Figure 5.
305 Fit parameters E, D_0, and r_0 and related errors for monovalent, divalent, trivalent, and tetravalent
306 cations in A, M1-M2-M3, and M4-M4' sites are reported in Table 5.

307

308 **Onuma diagrams for monovalent, divalent, trivalent, and tetravalent cations**

309 The partitioning behaviour for cations (D_i) with the same valence is conveniently shown in Onuma
310 diagrams (Onuma et al. 1968) as a function of the ionic radius, indicating which elements are
311 compatibles/incompatibles in a given site or which ones are fractionated between two distinct sites. The
312 parabolic fits of monovalent cations indicate that they are incorporated in the larger A-site permitting a

very good constraining of its lattice strain parameters, especially for APR16-ST1 run. The best fits for the monovalent cations of the runs APR16-C3Ad and APR16-C3Bd were obtained by fixing the E value equal to that determined by the fit of APR16-ST1.

The larger divalent elements (Ca, Sr, Pb, Ba) enter the XII-fold A-site, whereas smaller cations enter into the M4-site with Mg, Co, Fe, Mn that seem to be fractionated between the VIII-fold and the VI-fold sites, Ni enters exclusively into the smaller VI-fold site. However, given that cations entering in the M4 sites plot only on the right-limb of the parabola it is not possible to fully constrain these fits. Also, the limited amount of data for the larger divalent cations prevented us from deriving the parabolic fits for these elements (Fig. 5). The parabolic distribution of the trivalent (i.e., REE, Sc, Cr, and Al) partition coefficients indicates that amphiboles crystallized close to equilibrium conditions (Fig. 5). One of the three structurally distinct octahedral (VI-folds) sites, M1, M2, or M3 hosts Sc, Cr, and Al whereas the REEs enter all in the larger VIII-fold M4 and M4' sites. Given the apexes of the parabolic fits in all the runs are located near the ionic radius of Gd, the REEs should preferentially occupy the M4' site (Bottazzi et al. 1999; Tiepolo et al. 2000b). Europium partition coefficients fall on the parabolas of the REE showing that all Eu is trivalent. Finally, tetravalent cations are fractionated between the VIII-fold (U, Th) and the VI-fold sites (Ti, Zr, Hf), while pentavalent cations (i.e., Nb, Ta, V) enter the small VI-fold site.

Comparison with the parameterized lattice strain model for REE of Shimizu et al. (2017)

Shimizu et al. (2017) used previous published experimental REE and Y partitioning data between amphibole and silicate melt, the lattice strain model, and nonlinear least-squares regression method to parameterize key partitioning parameters in the lattice strain model for REEs as a function of pressure, temperature, and both amphibole and melt compositions. We compared our D_{REE} with those obtained applying the model (Hybrid mode using mineral and melt chemistry) of Shimizu et al. (2017). As

shown in Figure 6, $^{\text{Amph-glass}}D_{\text{REE}}$ predicted by Shimizu et al. (2017) correlates quite well with those measured in this study (R^2 = 0.68-0.74). In particular, the most compatible elements show a good agreement with the Shimizu et al. model while the elements that most differ from the model are the most incompatible ones (e.g., La, Ce). This deviation can be explained considering the analytical difficulties in measuring these incompatible elements due to possible micro/nano inclusion of glass and/or the limited spot size. Moreover, the combination of the small spot size (12 μm), used for the measurement of the trace element concentrations, with the potential presence of defect substitutions, kinetic effects and boundary layers in the melt can have a significant effect on the measurement error of the most incompatible elements making their analytical determination extremely difficult or impossible (Fabbrizio et al. 2021) .

Influence of melt composition, pressure, and temperature on trace element partitioning

To determine the main influencing variables affecting the partition coefficients (e.g., melt composition, Amph composition, temperature, pressure), we performed multiple linear regression analyses using our data joint to those of a database of existing experimental amphibole-melt partition coefficients (LEPR database and data from Nandedkar et al. 2016, Zhang et al. 2019, and Cannaò et al. 2022) spanning a wide range of conditions (0.6-2.5 GPa, 780-1100 °C; Table S3 of Supplementary Material 2) and starting compositions from basalt to rhyolite (Fig. S1 of Supplementary Material 1). The experiments crystallized calcic amphiboles in the range pargasite-edenite-hastingsite-magnesiohastingsite-magnesiohorneblende (Fig. S3 of Supplementary Material 1). In the regression analysis, the natural logarithms of $^{\text{Amph/L}}D$ ($\ln D$) were treated as independent variables while melt composition (X_{nf}/X), Amph composition ($Mg\#_{Amph}$), P, and T were considered as dependent variables. X_{nf}/X is defined as the sum of the molar fractions of network-forming cations (X_{nf}, i.e., Si and the fraction of Al balanced by alkalis) normalized to the sum of all cations on a molar basis (X; Tiepolo et al. 2000b), while

$Mg\#_{Amph}$ is defined as $Mg/(Mg+Fe^{2+}+Fe^{3+})$. Instead of the NBO/T value (i.e., NBOs are the non-bridging oxygen atoms and T are the cations in tetrahedral coordination) that is usually used to express the structural organization of a melt and requires the knowledge of the H_2O content and the Fe^{2+}/Fe^{3+} ratio of the melt, we decided to use the parameter X_{nf}/X because it allows making a wider comparison with the literature data for many of which H_2O content and Fe^{2+}/Fe^{3+} ratio data are missing. We obtained a fine correlation (R^2 >0.8) for Fe, Ho, Tb, and Tm (Figure 7 and Supplementary Material 3), whose partition coefficients are greatly influenced by X_{nf}/X, T and $Mg\#_{Amph}$. Particularly, Fe (R^2 = 0.83 and SEE = ± 18), Ho (R^2 = 0.87 and SEE = ± 4) and Tm (R^2 = 0.86 and SEE = ± 3) are affected by X_{nf}/X, *T* and $Mg\#_{Amph}$, while Tb (R^2 = 0.91 and SEE = ± 2) by X_{nf}/X and $Mg\#_{Amph}$. For Ca, Ce, Dy, Er, Eu, Gd, K, Lu, Mg, Mn, Nb, Nd, Pr, Sm, Ti, Yb (Supplementary Material 3) we obtained satisfactory correlation (R^2 = 0.7-0.8) observing, also in this case, the main influence of X_{nf}/X followed by $Mg\#_{Amph}$, P, and T. Finally, we observed a moderate correlation (R^2 = 0.6-0.7) for Al, Hf, La, Ta, Zr (Supplementary Material 3) while for the remaining elements (e.g., Ba, Cr, Na, Ni, Rb, Sr) we did not observe a clear trend (R^2 <0.5). As regards Pb, Th and U, instead, we noted the influence of X_{nf}/X, T and P, without finding any good correlations (R^2 ~0.5; Supplementary Material 3). We noticed, indeed, that our runs and those of Zhang et al. (2019) show higher $D_{Pb,}$ $D_{Th,}$ and D_U than those of the other data considered in the comparison. The observed variation may also be related either to melt polymerization either to the effect of the redox conditions on the oxidation state of U (Tiepolo et al. 2007). Whether or not the significant increase in $^{Amph/L}D_i$ for Pb, Th, and U is related to variations of melt structure, oxide phases crystallization or oxygen fugacity is beyond the scope of this study.

Melt composition. The influence of melt composition on partitioning is essentially related to its degree of polymerization: the higher the structural organization of the melt, the lower the probability of hosting those cations not fitting tetrahedral coordination due to their ionic radius and charge (Tiepolo et al. 2007). As shown in Supplementary Material 3, at X_{nf}/X ranging between 0.5 and 0.8, the relation

This is the peer-reviewed, final accepted version for American Mineralogist, published by the Mineralogical Society of America.
The published version is subject to change. Cite as Authors (Year) Title. American Mineralogist, in press.
DOI: https://doi.org/10.2138/am-2022-8536. http://www.minsocam.org/

between $^{Amph/L}D_{REE}$ and melt composition is approximately linear as observed in Tiepolo et al. (2000b). As regards HFSE, $^{Amph/L}D_{Ti}$ is exponentially correlated with melt composition (Supplementary Material 3). As observed also in the work of Tiepolo et al. (2007), at higher X_{nf}/X values (>0.6) the variation of $^{Amph/L}D_{Ti}$ with melt composition is stronger, and two separate trends can be distinguished. The first trend is similar to that observed for REE (Dy and Yb). The second trend, defined by the samples from Hilyard et al. (2000), Tiepolo et al. (2000a), Xiong et al. (2005), and Liu et al. (2015), in agreement with what previously observed in the work of Tiepolo et al. (2007), suggests the prevalence of structural control on $^{Amph/L}D$ for Ti^{4+} over that of the melt. A similar strong crystal structure control has been observed on $^{Amph/L}D_{Ca}$, $^{Amph/L}D_{Fe}$, $^{Amph/L}D_{K}$, $^{Amph/L}D_{Mg}$.

Pressure. The role of pressure on the $^{Amph/L}D$ of the LIL elements was specifically investigated by Adam and Green (1994) and Dalpé and Baker (2000). Dalpé and Baker (2000) noted that $^{Amph/L}D$ for the elements with ionic radii farther from the r_0 of the A-site are much more strongly affected by pressure than those with ionic radius closer to the r_0. The dependence of $^{Amph/L}D$ for Rb on pressure is much stronger than that of Na or K (Dalpé and Baker 2000). However, in this study, as possible to see for Ba in Supplementary Material 3, no obvious correlation between LILE and pressure can be noted. The effect of pressure on the overall variation of the $^{Amph/L}D_{REE}$ was investigated by Adam and Green (1994). These authors showed that $^{Amph/L}D$ for Lu and Sm decrease by up to a factor of about two with increasing pressure from 0.5 to 2.0 GPa. We observed a similar beahviour with a decrease of D_{REE} (La, Ce, Eu, Nd, Sm) with increasing pressure from 0.5 to 3 GPa in the comparison of our data with the database of existing experimental amphibole-melt partition coefficients (Supplementary Material 3). Adam and Green (2003) showed that the negative correlation observed between D_{REE} and pressure is not predicted by the thermodynamic model of Wood and Blundy (1997) and concluded that variations in $^{Amph/L}D_{REE}$ mostly depend on the volume-reducing substitutions occurring at the octahedra and the tetrahedra, which increase the activities of +3 and +4 ions, and decrease those of +1 ions, in sites with

VIII-fold co-ordination as pressure increases. A specific study on the influence of pressure on the $^{Amph/L}D_{HFSE}$ was carried out by Adam and Green (1994), who documented a decrease of the $^{Amph/L}D_{Ti}$ by a factor of 2 with increasing pressure from 0.5 to 2.0 GPa. According to this observation, we noted for the dataset considered, a decrease of D_{Ti}, D_{Zr}, and D_{Hf} with increasing pressure up to ~3 GPa for the considered data set.

Temperature. Adam and Green (1994) observed that *D*-values for Ti and REE are relatively insensitive to changes in temperature contrasting with the results of many previous studies (e.g., Nicholls and Harris 1980; Ray et al. 1983; Green and Pearson 1985). The reason for this is not immediately obvious but may be related to the complex inter-element substitutions which occur between crystallographic sites as temperature varies. Even the recent studies of Li et al. (2017) and Shimizu et al. (2017) observed the influence of temperature on trace element partitioning. Particularly, Li et al. (2017) observed a decrease of D_{Ti} and D_{Nb} with increasing temperature, while Shimizu et al. (2017) noticed that D_0 for REE negatively correlates with temperature. However, to date, the influence of temperature on amphibole/melt trace element partitioning has been found only in a few experimental works in the literature probably due to the relatively small thermal stability field of the amphibole and/or the relation between temperature and melt polymerization. Noteworthy, in the runs of this study we identified the influence of temperature on the partitioning of several trace elements between amphibole and melt, which can be well observed considering the D_0 values reported in Table 5. As regards the divalent cations, we noted that D_0 increases with decreasing T in M1-M2-M3 site while it decreases with decreasing T in M4-M4' one (Fig. 8a). This trend suggests that the decrease in T favors the entry of Mn, Fe, Co, Mg in VI-fold coordination into the M1-M2-M3 site. As regards the trivalent cations, we noted that D_0 decreases with decreasing T in M1-M2-M3 site while it increases with decreasing T in M4-M4' one (Fig. 8b). In this case, REEs are favored with respect to Al, Cr, Sc as the T decreases, in agreement with what was observed by Shimizu et al. (2017). Finally, as regards tetravalent cations (Ti,

433 Hf, Zr), D_0 tends to decrease with increasing T in M1-M2-M3 site (Fig. 8c), agreeing with what was
434 previously observed for D_{Ti} in the work of Li et al. (2017).
435 The trends of the D_0 for divalent, trivalent, and tetravalent cations in M1-M2-M3 and M4-M4' sites as
436 a function of temperature, observed in Figure 8, are well in agreement with the trends of the respective
437 D_i considered in the multiple linear regression (Supplementary Material 3). For instance, we noted a
438 positive correlation for D_{Al} (trivalent in M1-M2-M3), and a negative correlation for D_{Fe}, D_{Mg} (divalent
439 in M1-M2-M3), D_{Dy}, D_{Eu}, D_{Ho}, D_{Nd} (trivalent in M4-M4'), and D_{Ti}, D_{Hf} (tetravalent in M1-M2-M3).
440

441 **IMPLICATIONS**

442 A unique aspect of the investigated composition (a primitive K-basalt from the Campi Flegrei Volcanic
443 District) lies in the compositional evolution of its experimental liquids as a function of the amount of
444 water in the melt, which covers the field of basalt, trachybasalt, and shoshonite for water content <3
445 wt%, and that of basaltic andesite and andesite for water content >4 wt% (Perinelli et al. 2019),
446 approaching in term of major elements those of the 2 Ma old, calc-alkaline volcanic products found in
447 Parete and Castelvolturno bore-holes (north-west of Campi Flegrei; Beccaluva et al. 1991 and
448 references therein) (Fig. S4 of Supplementary Material 1). The trace element compositions of the
449 experimental residual glasses, on the other hand, do not correspond to those of the calc-alkaline rocks
450 of Campi Flegrei. This difference is not surprising because geochemical models of magmatic suites
451 deriving from metasomatic mantle sources should be computed on co-magmatic end-members (e.g.,
452 Gaeta et al. 2016, 2021) and ~2 Ma separate the APR16 basalt from the old calc-alkaline rocks of
453 Campi Flegrei. The presence of tephra dated at 2.214 ± 0.034 Ma and rich in amphibole with relative
454 high Mg# (60-64; Florindo et al. 2021; Fig. S5 of Supplementary Material 1) indicates, on the other
455 hand, the importance of the amphibole in the pre-eruptive systems of the volcanic districts of the
456 circum-Tyrrhenian region.

457 We used submarine basalt to trachybasalt compositions from the Pontine archipelago area to model the
458 trace element abundances due to the fractional crystallization of amphibole. These rocks have been
459 interpreted to be the primitive/intermediate lithologies representing parental compositions for the >1
460 Ma, peralkaline felsic rocks outcropping in the western Pontine Islands (Conte et al. 2016, 2020). In
461 addition, the Pontine submarine lithotypes share orogenic trace element signatures exhibited by the
462 calc-alkaline volcanic products of the Campi Flegrei. This and the results obtained from H_2O-saturated
463 experiments on APR16 prompted us to test the hypothesis whether a composition similar to those
464 submarine basalts, approaching that of APR16 (i.e., SiO_2 = 49.31-50.31 wt%, Na_2O+K_2O = 3.81-5.39
465 wt%, Mg# = 0.72-0.64; Conte et al. 2016, 2020), is able of producing andesites with the trace elements
466 abundances such as those recovered in the Parete and Castelvolturno bore-holes by a differentiation
467 process that involves the crystallization of amphibole. Thus, using as parental magma the trace element
468 composition of submarine TD4B basalt (Conte et al. 2016), we calculated the concentration of selected
469 elements in residual melts due to crystal-liquid fractionation process (FC). To model the FC process,
470 we used the Excel© spreadsheet program ‘‘FC-AFC-FCA and mixing modeler” (Ersoy and Helvaci
471 2010) considering: *i*) a fractionate mineral assemblage formed by amphibole + clinopyroxene + oxides
472 in proportion as in the experiments producing an andesitic residual melt (Table 2), *ii*) the partition
473 coefficients amphibole-melt determined in this study, *iii*) the partition coefficients clinopyroxene-melt
474 from the longest experiments determined by Bonechi et al. (2021). Modelling results indicate that the
475 pattern of natural andesite, is well reproduced for a calculated residual liquid fraction of 44% (Fig. 9), a
476 value close to the experimental 40% (Table 2), with the exception of Cs and Rb. As for Cs and Rb, the
477 fractionation behavior of these elements cannot be accurately modelled starting from TD4B basalt
478 composition. This result could be due either to the mobility and the incompatibility (D <1) of these
479 elements either to the presence of a parental magma with different Cs and Rb concentrations.
480

ACKNOWLEDGMENTS AND FUNDING

We warmly thank the reviewers K. Putirka and J. Brenan, for their very helpful, constructive and resolutive comments. The Editor, C. E. Lesher, is acknowledged for the editorial work. We thank M. Albano and M. Serracino (CNR-IGAG), R. Jedlicka and M. Racek (Institute of Petrology and Structural Geology, Charles University of Prague) for assistance during SEM and EPMA analytical sessions. This research has been conducted with the financial support of the HP-HT Laboratory at the Department of Earth Sciences of Sapienza - University of Rome. B.B. acknowledges financial support from “Fondi Avvio alla ricerca Tipo 2”.

REFERENCES CITED

Adam, J., and Green, T. (2003) The influence of pressure, mineral composition and water on trace element partitioning between clinopyroxene, amphibole and basanitic melts. European Journal of Mineralogy, 15, 831–841.

——— (2006) Trace element partitioning between mica- and amphibole-bearing garnet lherzolite and hydrous basanitic melt: 1. Experimental results and the investigation of controls on partitioning beahviour. Contributions to Mineralogy and Petrology 2006, 152, 1–17.

Adam, J., and Green, T.H. (1994) The effects of pressure and temperature on the partitioning of Ti, Sr and REE between amphibole, clinopyroxene and basanitic melts. Chemical Geology, 117, 219–233.

Adam, J., Green, T.H., and Sie, S.H. (1993) Proton microprobe determined partitioning of Rb, Sr, Ba, Y, Zr, Nb and Ta between experimentally produced amphiboles and silicate melts with variable F content. Chemical Geology, 109, 29–49.

503 Aigner-Torres, M., Blundy, J., Ulmer, P., and Pettke, T. (2007) Laser Ablation ICPMS study of trace
504 element partitioning between plagioclase and basaltic melts: An experimental approach.
505 Contributions to Mineralogy and Petrology, 153, 647–667.
506 Anders, E., and Grevesse, N. (1989) Abundances of the elements: Meteoritic and solar. Geochimica et
507 Cosmochimica Acta, 53, 197–214.
508 Barr, J.A., and Grove, T.L. (2010) AuPdFe ternary solution model and applications to understanding
509 the fO_2 of hydrous, high-pressure experiments. Contributions to Mineralogy and Petrology, 160,
510 631–643.
511 Beccaluva, L., Di Girolamo, P., and Serri, G. (1991) Petrogenesis and tectonic setting of the Roman
512 Volcanic Province. Lithos, 26, 191–221.
513 Blundy, J.D., and Wood, B.J. (1994) Prediction of crystal-melt partition coefficients from elastic
514 moduli. Nature, 372, 452–454.
515 ——— (2003) Partitioning of trace elements between crystals and melts. Earth and Planetary Science
516 Letters, 210, 383–397.
517 Bonechi, B. (2020) Influence of pre-existing nuclei on the crystallization kinetics of primitive alkaline
518 magmas: Insights on the deep feeding system of the campi flegrei Volcanic district. Minerals, 10,
519 234.
520 Bonechi, B., Perinelli, C., Gaeta, M., Tecchiato, V., and Granati, S.F. (2017) Experimental constraints
521 on amphibole stability in primitive alkaline and calc-alkaline magmas. Periodico di Mineralogia,
522 86, 231–245.
523 Bonechi, B., Perinelli, C., Gaeta, M., Tecchiato, V., and Fabbrizio, A. (2020a) Amphibole growth from
524 a primitive alkaline basalt at 0.8 GPa: time-dependent compositional evolution, growth rate and
525 competition with clinopyroxene. Lithos, 354–355, 105272.

526 Bonechi, B., Perinelli, C., and Gaeta, M. (2020b) Clinopyroxene growth rates at high pressure:
527 constraints on magma recharge of the deep reservoir of the Campi Flegrei Volcanic District (south
528 Italy). Bulletin of Volcanology, 82, 5.
529 Bonechi, B., Perinelli, C., Gaeta, M., Fabbrizio, A., Petrelli, M., and Strnad, L. (2021) High pressure
530 trace element partitioning between clinopyroxene and alkali basaltic melts. Geochimica et
531 Cosmochimica Acta, 305, 282–305.
532 Bottazzi, P., Tiepolo, M., Vannucci, R., Zanetti, A., Brumm, R., Foley, S.F., and Oberti, R. (1999)
533 Distinct site preferences for heavy and light REE in amphibole and the prediction of
534 (Amph/L)D(REE). Contributions to Mineralogy and Petrology, 137, 36–45.
535 Brenan, J.M., Shaw, H.F., Ryerson, F.J., and Phinney, D.L. (1995) Experimental determination of
536 trace-element partitioning between pargasite and a synthetic hydrous andesitic melt. Earth and
537 Planetary Science Letters, 135, 1–11.
538 Brenan, J.M., Neroda, E., Lundstrom, C.C., Shaw, H.F., Rverson, F.J., and Phinney, D.L. (1998)
539 Behaviour of boron, beryllium, and lithium during melting and crystallization: constraints from
540 mineral-melt partitioning experiments. Geochimica et Cosmochimica Acta, 62, 2129–2141.
541 Brice, J.C. (1975) Some thermodynamic aspects of the growth of strained crystals. Journal of Crystal
542 Growth, 28, 249–253.
543 Cannaò, E., Tiepolo, M., Borghini, G., Langone, A., and Fumagalli, P. (2022) The influence of oxygen
544 fugacity and chlorine on amphibole-liquid trace element partitioning at upper-mantle conditions.
545 European Journal of Mineralogy, 34, 35–57.
546 Conte, A.M., Dolfi, D., Gaeta, M., Misiti, V., Mollo, S., and Perinelli, C. (2009) Experimental
547 constraints on evolution of leucite-basanite magma at 1 and 10^{-4} GPa : implications for parental
548 compositions of Roman high-potassium magmas. European Journal of Mineralogy, 21, 763–782.

549 Conte, A.M., Perinelli, C., Bianchini, G., Natali, C., Martorelli, E., and Chiocci, F.L. (2016) New
550 insights on the petrology of submarine volcanics from the Western Pontine Archipelago
551 (Tyrrhenian Sea, Italy). Journal of Volcanology and Geothermal Research, 327, 223–239.
552 Conte, A.M., Perinelli, C., Bosman, A., Castorina, F., Conti, A., Cuffaro, M., Di Vincenzo, G.,
553 Martorelli, E., and Bigi, S. (2020) Tectonics, Dynamics, and Plio-Pleistocene Magmatism in the
554 Central Tyrrhenian Sea: Insights From the Submarine Transitional Basalts of the Ventotene
555 Volcanic Ridge (Pontine Islands, Italy). Geochemistry, Geophysics, Geosystems, 21,
556 e2020GC009346.
557 D'Antonio, M., Civetta, L., and Di Girolamo, P. (1999) Mantle source heterogeneity in the Campanian
558 Region (South Italy) as inferred from geochemical and isotopic features of mafic volcanic rocks
559 with shoshonitic affinity. Mineralogy and Petrology, 67, 163–192.
560 Dalou, C., Boulon, J., T. Koga, K., Dalou, R., and Dennen, R.L. (2018) DOUBLE FIT: Optimization
561 procedure applied to lattice strain model. Computers and Geosciences, 117, 49–56.
562 Dalpé, C., and Baker, D.R. (2000) Experimental investigation of large-ion-lithophile-element-, high-
563 field-strength-element- and rare-earth-element-partitioning between calcic amphibole and basaltic
564 melt: The effects of pressure and oxygen fugacity. Contributions to Mineralogy and Petrology,
565 140, 233–250.
566 De Astis, G., Pappalardo, L., and Piochi, M. (2004) Procida volcanic history: New insights into the
567 evolution of the Phlegraean Volcanic District (Campania region, Italy). Bulletin of Volcanology,
568 66, 622–641.
569 Devine, J.D., Gardner, J.E., Brack, H.P., Layne, G.D., and Rutherford, M.J. (1995) Comparison of
570 microanalytical methods for estimating H_2O contents of silicic volcanic glasses. American
571 Mineralogist, 80, 319–328.

572 Dostal, J., Dupuy, C., Carron, J.P., Le Guen de Kerneizon, M., and Maury, R.C. (1983) Partition
573 coefficients of trace elements: Application to volcanic rocks of St. Vincent, West Indies.
574 Geochimica et Cosmochimica Acta, 47, 525–533.
575 Draper, D., and van Westrenen, W. (2007) Quantifying garnet-melt trace element partitioning using
576 lattice-strain theory: assessment of statistically significant controls and a new predictive model.
577 Contributions to Mineralogy and Petrology, 154, 731–746.
578 Ersoy, Y., and Helvaci, C. (2010) FC-AFC-FCA and mixing modeler: A Microsoft® Excel©
579 spreadsheet program for modeling geochemical differentiation of magma by crystal fractionation,
580 crustal assimilation and mixing. Computers and Geosciences, 36, 383–390.
581 Fabbrizio, A., Schmidt, M.W., Günther, D., and Eikenberg, J. (2008) Experimental determination of
582 radium partitioning between leucite and phonolite melt and ^{226}Ra-disequilibrium crystallization
583 ages of leucite. Chemical Geology, 255, 377–387.
584 ——— (2009) Experimental determination of Ra mineral/melt partitioning for feldspars and 226Ra-
585 disequilibrium crystallization ages of plagioclase and alkali-feldspar. Earth and Planetary Science
586 Letters, 280, 137–148.
587 ——— (2010) Ra-partitioning between phlogopite and silicate melt and ^{226}Ra/Ba-^{230}Th/Ba isochrons.
588 Lithos, 114, 121–131.
589 Fabbrizio, A., Schmidt, M.W., and Petrelli, M. (2021) Effect of fO_2 on Eu partitioning between
590 clinopyroxene, orthopyroxene and basaltic melt: Development of a Eu^{3+}/Eu^{2+} oxybarometer.
591 Chemical Geology, 559, 119967.
592 Florindo, Fabio, Marra, F., Angelucci, D.E., Biddittu, I., Bruni, L., Florindo, Federico, Gaeta, M.,
593 Guillou, H., Jicha, B., Macrì, P., and others (2021) Environmental evolution, faunal and human
594 occupation since 2 Ma in the Anagni basin, central Italy. Scientific Reports, 11, 1–17.

595 Freda, C., Baker, D.R., and Ottolin, L. (2001) Reduction of water loss from gold-palladium capsules
596 during piston-cylinder experiments by use of pyrophyllite powder. American Mineralogist, 86,
597 234–237.
598 Gaeta, M., Freda, C., Marra, F., Arienzo, I., Gozzi, F., Jicha, B., and Di Rocco, T. (2016) Paleozoic
599 metasomatism at the origin of Mediterranean ultrapotassic magmas: Constraints from time-
600 dependent geochemistry of Colli Albani volcanic products (Central Italy). Lithos, 244, 151–164.
601 Gaeta, M., Bonechi, B., Marra, F., and Perinelli, C. (2021) Uncommon K-foiditic magmas: The case
602 study of Tufo del Palatino (Colli Albani Volcanic District, Italy). Lithos, 396–397, 106239.
603 Green, T.H., and Pearson, N.J. (1985) Rare earth element partitioning between clinopyroxene and
604 silicate liquid at moderate to high pressure. Contributions to Mineralogy and Petrology, 91, 24–36.
605 Hawthorne, F.C., Oberti, R., Harlow, G.E., Maresch, W. V, Martin, R.F., Schumacher, J.C., and
606 Welch, M.D. (2012) Nomenclature of the amphibole supergroup. American Mineralogist, 97,
607 2031–2048.
608 Hill, E., Blundy, J.D., and Wood, B.J. (2011) Clinopyroxene-melt trace element partitioning and the
609 development of a predictive model for HFSE and Sc. Contributions to Mineralogy and Petrology,
610 161, 423–438.
611 Hilyard, M., Nielsen, R.L., Beard, J.S., Patinõ-Douce, A., and Blencoe, J. (2000) Experimental
612 determination of the partitioning behavior of rare earth and high field strength elements between
613 pargasitic amphibole and natural silicate melts. Geochimica et Cosmochimica Acta, 64, 1103–
614 1120.
615 Hughes, E.C., Buse, B., Kearns, S.L., Blundy, J.D., Kilgour, G.N., and Mader, H.M. (2019) Low
616 analytical totals in EPMA of hydrous silicate glass due to sub-surface charging: Obtaining
617 accurate volatiles by difference. Chemical Geology, 505, 48–56.

618 Humphreys, M.C.S., Kearns, S.L., and Blundy, J.D. (2006) SIMS investigation of electron-beam
619 damage to hydrous, rhyolitic glasses: implications for melt inclusion analysis. American
620 Mineralogist, 91, 667–679.
621 Icenhower, J., and London, D. (1996) Experimental partitioning of Rb, Cs, Sr, and Ba between alkali
622 feldspar and peraluminous melt. American Mineralogist, 81, 719–734.
623 Irvine, T.N., and Baragar, W.R.A. (1971) A Guide to the Chemical Classification of the Common
624 Volcanic Rocks. Canadian Journal of Earth Sciences, 8, 523-548.
625 Johannes, W., Bell, P.M., Mao, H.K., Boettcher, A.L., Chipman, D.W., Hays, J.F., Newton, R.C., and
626 Seifert, F. (1971) An interlaboratory comparison of piston-cylinder pressure calibration using the
627 albite-breakdown reaction. Contributions to Mineralogy and Petrology, 32, 24–38.
628 Klein, M., Stosch, H.G., and Seek, H.A. (1997) Partitioning of high field-strength and rare-earth
629 elements between amphibole and quartz-dioritic to tonalitic melts: an experimental study.
630 Chemical Geology, 138, 257–271.
631 LaTourrette, T., Hervig, R.L., and Holloway, J.R. (1995) Trace element partitioning between
632 amphibole, phlogopite, and basanite melt. Earth and Planetary Science Letters, 135, 13–30.
633 Le Bas, M.J., W, L.M.R., Streckeisen, A., and Zanettin, B. (1986) A chemical classification of volcanic
634 rocks based on the total alkali-silica diagram. Journal of Petrology, 27, 745-750.
635 Li, L., Xiong, X.L., and Liu, X.C. (2017) Nb/Ta fractionation by amphibole in hydrous basaltic
636 systems: Implications for arc magma evolution and continental crust formation. Journal of
637 Petrology, 58, 328.
638 Liu, X., Xiong, X., Audétat, A., and Li, Y. (2015) Partitioning of Cu between mafic minerals, Fe–Ti
639 oxides and intermediate to felsic melts. Geochimica et Cosmochimica Acta, 151, 86–102.
640 Mazzeo, F.C., D'Antonio, M., Arienzo, I., Aulinas, M., Di Renzo, V., and Gimeno, D. (2014)
641 Subduction-related enrichment of the Neapolitan volcanoes (Southern Italy) mantle source: New

642 constraints on the characteristics of the slab-derived components. Chemical Geology, 386, 165–
643 183.
644 McDonough, W.F., and Sun, S. s. (1995) The composition of the Earth. Chemical Geology, 120, 223–
645 253.
646 Mollo, S., Blundy, J., Scarlato, P., De Cristofaro, S.P., Tecchiato, V., Di Stefano, F., Vetere, F., Holtz,
647 F., and Bachmann, O. (2018) An integrated P-T-H_2O-lattice strain model to quantify the role of
648 clinopyroxene fractionation on REE+Y and HFSE patterns of mafic alkaline magmas: Application
649 to eruptions at Mt. Etna. Earth-Science Reviews, 185, 32-56.
650 Morabito, S., Petrosino, P., Milia, A., Sprovieri, M., and Tamburrino, S. (2014) A multidisciplinary
651 approach for reconstructing the stratigraphic framework of the last 40 ka in a bathyal area of the
652 eastern Tyrrhenian Sea. Global and Planetary Change, 123, 121–138.
653 Nandedkar, R.H., Hürlimann, N., Ulmer, P., and Müntener, O. (2016) Amphibole-melt trace element
654 partitioning of fractionating calc-alkaline magmas in the lower crust: an experimental study.
655 Contributions to Mineralogy and Petrology, 171, 71.
656 Nicholls, I.A., and Harris, K.L. (1980) Experimental rare earth element partition coefficients for garnet,
657 clinopyroxene and amphibole coexisting with andesitic and basaltic liquids. Geochimica et
658 Cosmochimica Acta, 44, 287–308.
659 Nielsen, R.L., and Ustunisik, G.K. (2019) Amphibole/melt partition coefficient experiments, Version
660 1.0. Interdisciplinary Earth Data Alliance (IEDA). https://doi.org/10.1594/IEDA/111286.
661 Onuma, N., Higuchi, H., Wakita, H., and Nagasawa, H. (1968) Trace element partition between two
662 pyroxenes and the host lava. Earth and Planetary Science Letters, 5, 47–51.
663 Perinelli, C., Gaeta, M., Bonechi, B., Granati, S.F., Freda, C., D'Antonio, M., Stagno, V., Sicola, S.,
664 and Romano, C. (2019) Effect of water on the phase relations of primitive K-basalts: Implications

665 for high-pressure differentiation in the Phlegraean Volcanic District magmatic system. Lithos,
666 342–343, 530–541.
667 Petrelli, M., Caricchi, L., and Ulmer, P. (2007) Application of high spatial resolution laser ablation
668 ICP-MS to crystal-melt trace element partition coefficient determination. Geostandards and
669 Geoanalytical Research, 31, 13–25.
670 Petrelli, M., Perugini, D., Alagna, K.E., Poli, G., and Peccerillo, A. (2008) Spatially resolved and bulk
671 trace element analysis by laser ablation - Inductively coupled plasma - Mass spectrometry (LA-
672 ICP-MS). Periodico di Mineralogia, 77, 3–21.
673 Petrelli, M., Laeger, K., and Perugini, D. (2016) High spatial resolution trace element determination of
674 geological samples by laser ablation quadrupole plasma mass spectrometry: implications for glass
675 analysis in volcanic products. Geosciences Journal, 20, 851–863.
676 Presnall, D.C., Dixon, S.A., Dixon, J.R., O'Donnell, T.H., Brenner, N.L., Schrock, R.L., and Dycus,
677 D.W. (1978) Liquidus phase relations on the join diopside-forsterite-anorthite from 1 atm to 20
678 kbar: Their bearing on the generation and crystallization of basaltic magma. Contributions to
679 Mineralogy and Petrology, 66, 203–220.
680 Putirka, K.D., Mikaelian, H., Ryerson, F., and Shaw, H. (2003) New clinopyroxene-liquid
681 thermobarometers for mafic, evolved, and volatile-bearing lava compositions, with applications to
682 lavas from Tibet and the Snake River Plain, Idaho. American Mineralogist, 88, 1542-1554.
683 Putirka, K.D. (2016) Amphibole thermometers and barometers for igneous systems and some
684 implications for eruption mechanisms of felsic magmas at arc volcanoes. American Mineralogist,
685 101, 841–858.
686 Ray, G.L., Shimizu, N., and Hart, S.R. (1983) An ion microprobe study of the partitioning of trace
687 elements between clinopyroxene and liquid in the system diopside-albite-anorthite. Geochimica et
688 Cosmochimica Acta, 47, 2131–2140.

689 Rawlings, J.O., Pantula, S.G., and Dickey, A.D. (1998) Applied Regression Analysis: A Research
690 Tool, Second Edition, Springer, New York, 17-18.
691 Ridolfi, F., Zanetti, A., Renzulli, A., Perugini, D., Holtz, F., and Oberti, R. (2018) AMFORM, a new
692 mass-based model for the calculation of the unit formula of amphiboles from electron microprobe
693 analyses. American Mineralogist, 103, 1112-1125.
694 Schmidt, K.H., Bottazzi, P., Vannucci, R., and Mengel, K. (1999) Trace element partitioning between
695 phlogopite, clinopyroxene and leucite lamproite melt. Earth and Planetary Science Letters, 168,
696 287–299.
697 Severs, M.J., Beard, J.S., Fedele, L., Hanchar, J.M., Mutchler, S.R., and Bodnar, R.J. (2009)
698 Partitioning behavior of trace elements between dacitic melt and plagioclase, orthopyroxene, and
699 clinopyroxene based on laser ablation ICPMS analysis of silicate melt inclusions. Geochimica et
700 Cosmochimica Acta, 73, 2123–2141.
701 Shannon, B.Y.R.D. (1976) Revised Effective Ionic Radii and Systematic Studies of Interatomie
702 Distances in Halides and Chaleogenides. Acta Crystallographica, A32, 751.
703 Shimizu, K., Liang, Y., Sun, C., Jackson, C.R.M., and Saal, A.E. (2017) Parameterized lattice strain
704 models for REE partitioning between amphibole and silicate melt. American Mineralogist, 102,
705 2254–2267.
706 Sisson, T.W. (1994) Hornblende-melt trace-element partitioning measured by ion microprobe.
707 Chemical Geology, 117, 331–344.
708 Storn, R., and Price, K. (1997) Differential Evolution - A Simple and Efficient Heuristic for Global
709 Optimization over Continuous Spaces. Journal of Global Optimization, 11, 341–359.
710 Sun, C., and Liang, Y. (2012) Distribution of REE between clinopyroxene and basaltic melt along a
711 mantle adiabat: Effects of major element composition, water, and temperature. Contributions to
712 Mineralogy and Petrology, 163, 807–823.

——— (2013) The importance of crystal chemistry on REE partitioning between mantle minerals (garnet, clinopyroxene, orthopyroxene, and olivine) and basaltic melts. Chemical Geology, 358, 23–36.

Tiepolo, M., Zanetti, A., and Oberti, R. (1999) Detection, crystal-chemical mechanisms and petrological implications of $^{[6]}Ti^{4+}$ partitioning in pargasite and kaersutite. European Journal of Mineralogy, 345–354.

Tiepolo, M., Vannucci, R., Oberti, R., Foley, S., Bottazzi, P., and Zanetti, A. (2000a) Nb and Ta incorporation and fractionation in titanian pargasite and kaersutite: crystal–chemical constraints and implications for natural systems. Earth and Planetary Science Letters, 176, 185–201.

Tiepolo, M., Vannucci, R., Bottazzi, P., Oberti, R., Zanetti, A., and Foley, S. (2000b) Partitioning of rare earth elements, Y, Th, U, and Pb between pargasite, kaersutite, and basanite to trachyte melts: Implications for percolated and veined mantle. Geochemistry, Geophysics, Geosystems, 1, 8.

Tiepolo, M., Oberti, R., Zanetti, A., Vannucci, R., and Foley, S.F. (2007) Trace-Element Partitioning Between Amphibole and Silicate Melt. Reviews in Mineralogy and Geochemistry, 67, 417-452.

van Kan Parker, M., Liebscher, A., Frei, D., van Sijl, J., van Westrenen, W., Blundy, J., and Franz, G. (2010) Experimental and computational study of trace element distribution between orthopyroxene and anhydrous silicate melt: Substitution mechanisms and the effect of iron. Contributions to Mineralogy and Petrology, 159, 459–473.

van Westrenen, W., and Draper, D.S. (2007) Quantifying garnet-melt trace element partitioning using lattice-strain theory: new crystal-chemical and thermodynamic constraints. Contributions to Mineralogy and Petrology, 154, 717–730.

Wan, F., Zhou, W., Jiang, N., Fan, D., Chen, H., and Xie, H. (2009) The partition characteristic of trace elements in the partial melting massive amphibolite at 1.5 GPa and 950 °C. Earth Science Frontiers, 16, 125–133.

Watson, E., Wark, D., Price, J., and Van Orman, J. (2002) Mapping the thermal structure of solid-media pressure assemblies. Contributions to Mineralogy and Petrology, 142, 640–652.

Weaver, S.L., Wallace, P.J., and Johnston, A.D. (2013) Experimental constraints on the origins of primitive potassic lavas from the Trans-Mexican Volcanic Belt. Contributions to Mineralogy and Petrology, 166, 825–843.

Wood, B.J., and Blundy, J.D. (1997) A predictive model for rare earth element partitioning between clinopyroxene and anhydrous silicate melt. Contributions to Mineralogy and Petrology, 129, 166–181.

——— (2001) The effect of cation on crystal-melt partitioning of trace elements. Earth and Planetary Science Letters, 188, 59–71.

Xiong, X.L., Adam, J., and Green, T.H. (2005) Rutile stability and rutile/melt HFSE partitioning during partial melting of hydrous basalt: Implications for TTG genesis. Chemical Geology, 218, 339–359.

Zanetti, A., Tiepolo, M., Oberti, R., and Vannucci, R. (2004) Trace-element partitioning in olivine: Modelling of a complete data set from a synthetic hydrous basanite melt. Lithos, 75, 39–54.

Zhang, B., Hu, X., Li, P., Tang, Q., and Zhou, W. (2019) Trace element partitioning between amphibole and hydrous. Acta Geochimica, 38, 414–429.

Figures captions

Figure 1. Backscattered images of experimental samples. Details of the experimental conditions are reported at the bottom of each image. Amph shows euhedral habit and maximum size of ~40 μm; pyroxene and oxide show euhedral habit with sizes up to ~5 μm and 40 μm, respectively. In Figure 1a some tiny quench crystals are present. Black holes with size ≤5 μm are saturation bubbles. Abbreviation: Amph: amphibole; Px: pyroxene; Ox: oxide; Gl: glass.

761 **Figure 2.** C1-normalized (Anders and Grevesse 1989) trace elements abundances for synthetic
762 amphiboles. C3A suite (1080 °C) is reported in green, C3B (1030 °C) in light blue and APR16-ST1
763 (1050 °C) in blue. Symbols indicate different experimental dwell time: circle 0.15 h, asterisk 2 h,
764 triangle 3 h, diamond 6 h and square 9 h.

765 **Figure 3.** C1-normalized (Anders and Grevesse 1989) trace elements abundances for analysed
766 synthetic glasses. Symbols are as in Figure 2. Red crosses indicate data for the APR16 natural samples
767 from Mazzeo et al. (2014). For comparison we reported C1-normalized trace elements abundances for
768 synthetic glasses of Bonechi et al. (2021), indicated with the yellow field.

769 **Figure 4.** Calculated $^{\text{Amph/Glass}}D$ values for trace elements in experimental samples. Symbols are as in
770 Figure 2.

771 **Figure 5.** Onuma diagrams for amphibole-liquid partition coefficients for mono-, di-, tri-, and
772 tetravalent cations versus ionic radii (in Å; Shannon 1976) for VI-, VIII- and XII-fold coordinated sites
773 along with the results of the lattice strain fits in A, M1-M2-M3, M4-M4' sites for samples (a) APR16-
774 C3Ad (1080 °C), (b) APR16-C3Bd (1030 °C), (c) APR16-ST1 (1050 °C). The dotted curves represent
775 the fits of the lattice strain model to $^{\text{Amph/Glass}}D_{\text{i}}$ values while symbols represent measured $^{\text{Amph/Glass}}D_{\text{i}}$
776 values. Cations are indicated as follow: monovalent in orange, divalent in green, trivalent in light blue,
777 tetravalent in yellow and pentavalent in purple. Cations in site-A are indicated with triangles, in site
778 M4-M4' with circles and in site M1-M2-M3 with squares. Empty symbols indicate elements not
779 considered in the fits of the LSM.

780 **Figure 6.** (a) Amphibole-melt REE partition coefficients calculated in this study and those calculated
781 using the model of Shimizu et al. (2017). Symbols are as in Figure 2. Solid lines indicates partition
782 coefficients calculated in this study while dashed lines those obtained with the model. (b) Comparison
783 between the experimentally measured partition coefficients to those predicted using the model of
784 Shimizu et al. (2017). The solid line represents 1:1 ratio, and dashed lines represent 2:1 and 1:2 ratios.

785 **Figure 7.** Calculated and predicted lnD_{Tb} is compared for the available database of existing
786 experimental amphibole-melt partition coefficients (LEPR database and data from Nandedkar et al.
787 2016, Zhang et al. 2019, and Cannaò et al. 2022; Table S3 of Supplementary Material 2 and
788 Supplementary Material 3). Solid and dashed grey lines are 1:1, 1:2 and 2:1 lines, while green dashed
789 line is the regression line. Embedded table reports the parameters and related errors obtained from the
790 regression analysis. For creating the model and to avoid over-fitting of the data the t-stat (calculated as
791 the ratios between the coefficients and their standard errors and thus representing a measure of the
792 precision with which the regression coefficients are measured; e.g., Rawlings et al. (1998)) were
793 checked for all variables, looking for the t-stat ≥ 5, and the P-value (a measure of how the overall result
794 of the regression is statistically significant; e.g., Rawlings et al. (1998)) was checked in order to
795 achieve the maximum value similarly to the approach used in Putirka et al. (2003).
796 **Figure 8.** Diagrams showing the variation in the strain-free partition coefficient (D_0) for the amphibole
797 as function of temperature for divalent (a), trivalent (b) and tetravalent (c) cations in VI-fold
798 coordinated M1-M2-M3 site and in VII-fold coordinated M4-M4' site. Symbols are as in Figure 5.
799 Arrows indicate the trends observed for D_0 as function of temperature variation.
800 **Figure 9.** Primitive Mantle normalized (McDonough and Sun 1995) trace elements patterns of TD4B
801 basalt (Conte et al. 2016) and the predicted composition of differentiated melts obtained after 56% of
802 fractional crystallization of TD4B basalt assumed as primitive parental melt of andesitic magma of
803 Campi Flegrei (sample from Parete borehole; Beccaluva et al. 1991). The reported degree of
804 fractionation (FC) reflects the crystallized phase assemblage and proportions determined for run
805 APR16-C3Bd (amphibole (35) + clinopyroxene (24) + oxide (1)) that produced andesitic residual glass.
806 The modelled compositions were calculated by using the Excel® spreadsheet program of Ersoy and
807 Helvaci (2010).
808

809

810 **Tables captions**

811 **Table 1** Composition (wt%) of APR16 rock sample and APR16GL starting material

812 **Table 2** Experimental run conditions, melt water contents, phases assemblage and proportions in run
813 products

814 **Table 3** Major and trace element concentrations (ppm) for synthetic amphibole crystals and glasses

815 **Table 4** Major and trace elements partition coefficients between amphibole and glass for experimental
816 samples

817 **Table 5** Best fits for E, r_0 and D_0 obtained by regression of amphibole/glass partition coefficients of
818 monovalent, divalent, trivalent and tetravalent cations in A, M1-M2-M3, M4-M4' sites

819

820 **Supplementary materials**

821 **Supplementary Material 1** contains supplementary figures

822 **Supplementary Material 2** contains supplementary tables

823 **Supplementary Material 3** contains multiple linear regression analyses

Figure 1

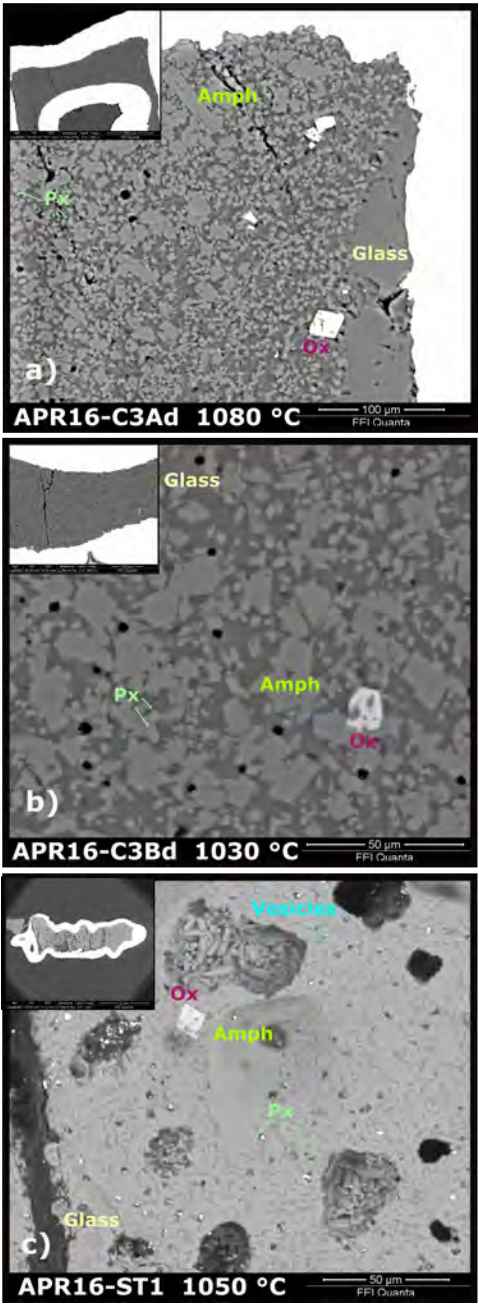
Amph
Px
Glass
Ox
a)
APR16-C3Ad 1080 °C
100 µm
FEI Quanta
Glass
Px
Amph
Ox
b)
APR16-C3Bd 1030 °C
50 µm
FEI Quanta
Vesicles
Ox
Amph
Px
Glass
c)
APR16-ST1 1050 °C
50 µm
FEI Quanta

Figure 2

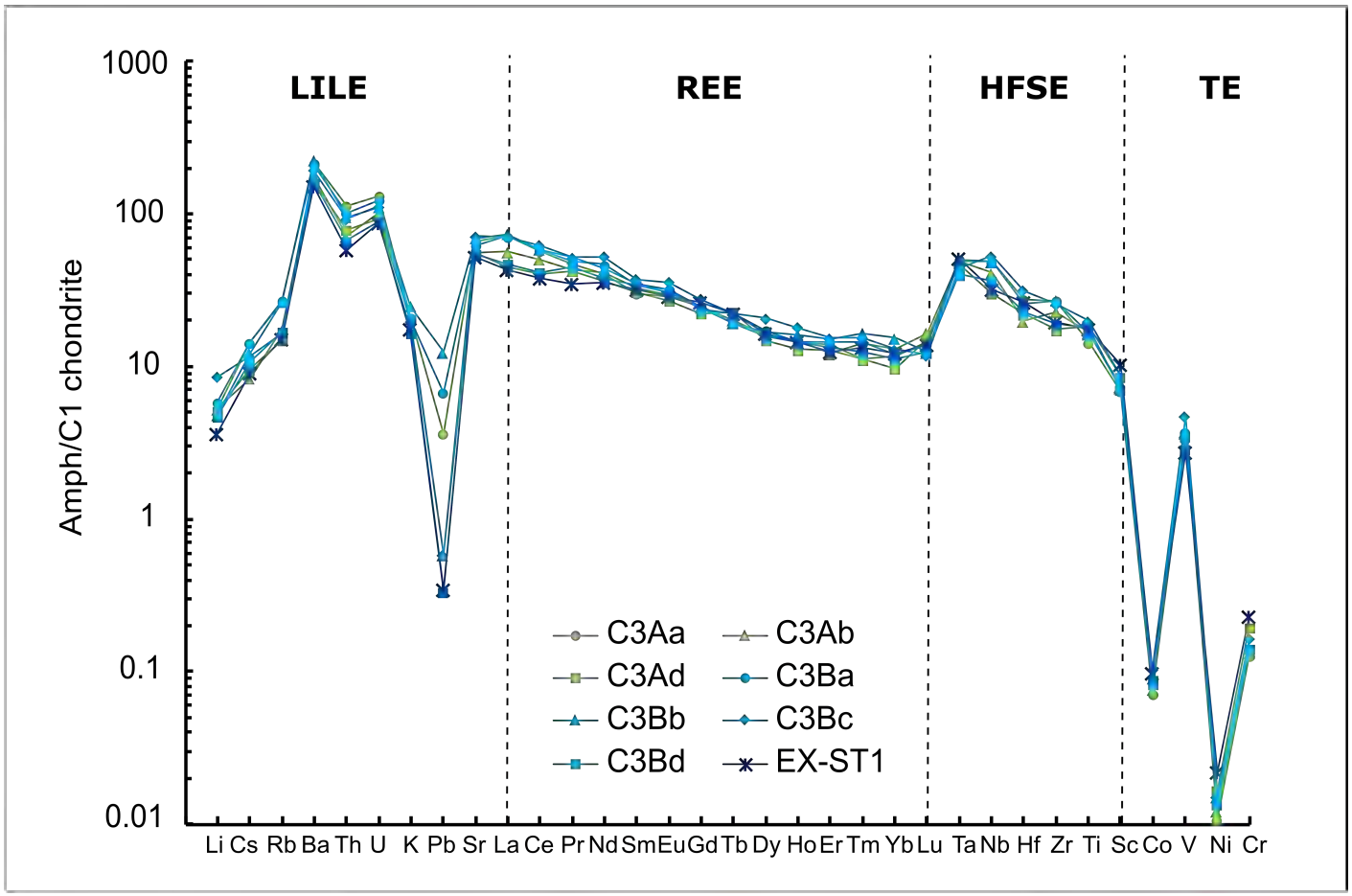
LILE
REE
HFSE
TE
1000
100
10
1
0.1
0.01
Amph/C1 chondrite
C3Aa
C3Ab
C3Ad
C3Ba
C3Bb
C3Bc
C3Bd
EX-ST1
Li Cs Rb Ba Th U K Pb Sr La Ce Pr Nd Sm Eu Gd Tb Dy Ho Er Tm Yb Lu Ta Nb Hf Zr Ti Sc Co V Ni Cr

Figure 3

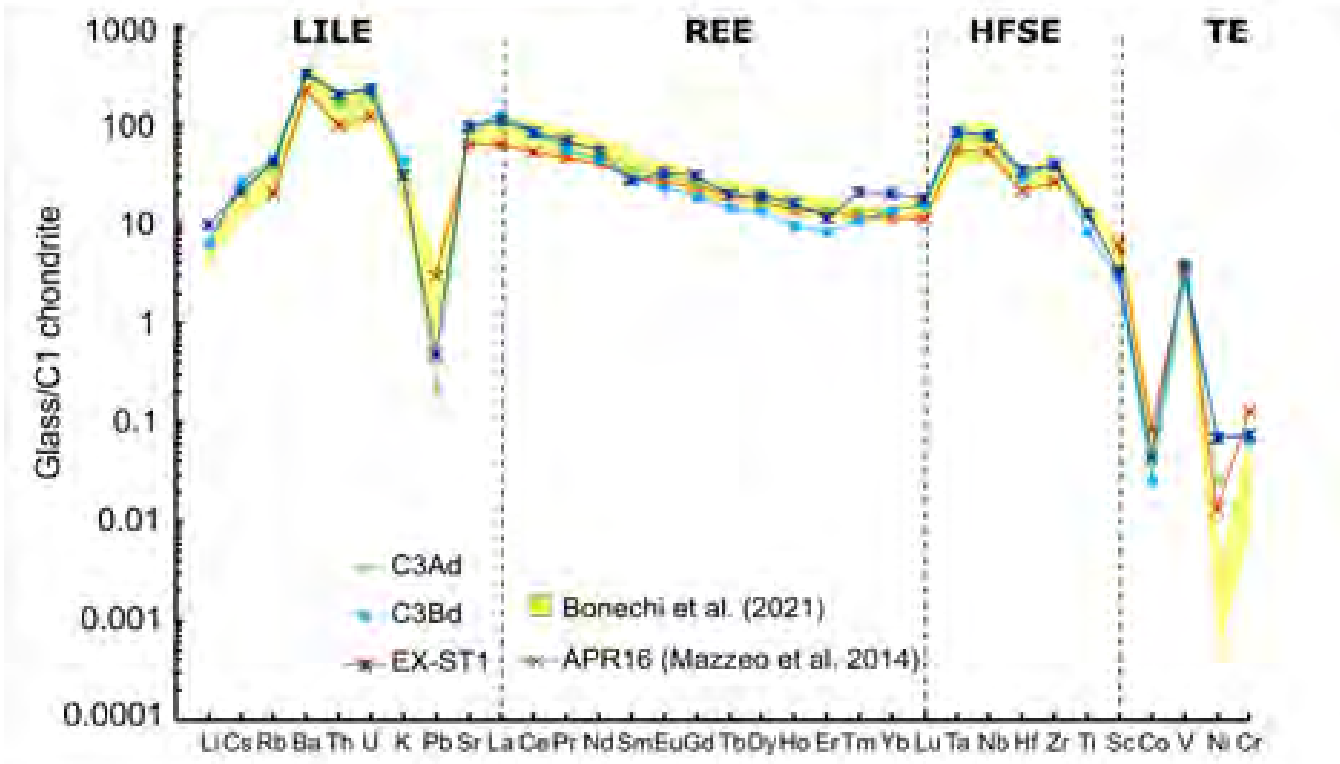
LILE
REE
HFSE
TE
1000
100
10
1
0.1
0.01
0.001
0.0001
Glass/C1 chondrite
C3Ad
C3Bd
EX-ST1
Bonechi et al. (2021)
APR16 (Mazzeo et al. 2014)
Li Cs Rb Ba Th U K Pb Sr La Ce Pr Nd Sm Eu Gd Tb Dy Ho Er Tm Yb Lu Ta Nb Hf Zr Ti Sc Co V Ni Cr

Figure 4

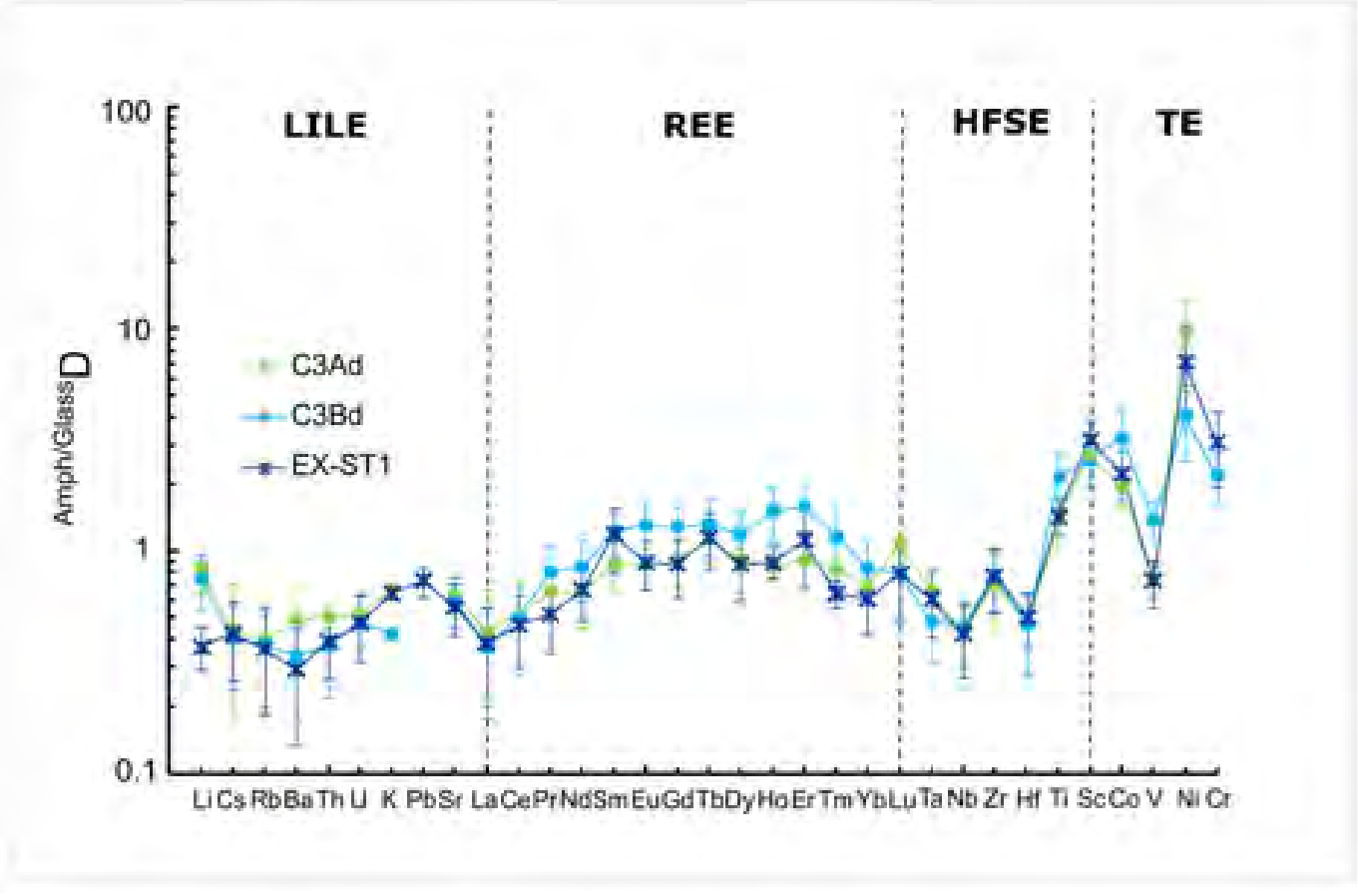
LILE
REE
HFSE
TE
100
10
1
0.1
Amph/Glass D
C3Ad
C3Bd
EX-ST1
Li Cs Rb Ba Th U K Pb Sr La Ce Pr Nd Sm Eu Gd Tb Dy Ho Er Tm Yb Lu Ta Nb Zr Hf Ti Sc Co V Ni Cr

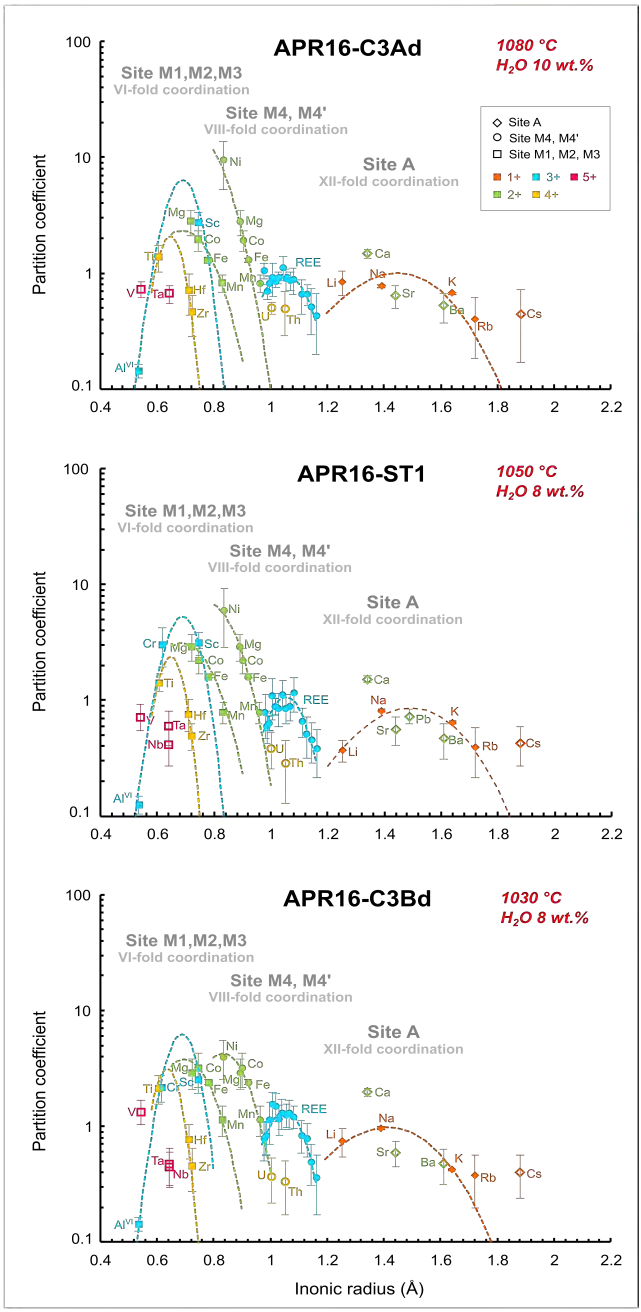
APR16-C3Ad
1080 °C
H2O 10 wt.%
Site M1,M2,M3
VI-fold coordination
Site M4, M4'
VIII-fold coordination
Site A
XII-fold coordination
Site A
Site M4, M4'
Site M1, M2, M3
1+
3+
5+
2+
4+
Partition coefficient
APR16-ST1
1050 °C
H2O 8 wt.%
APR16-C3Bd
1030 °C
H2O 8 wt.%
Inonic radius (Å)

Figure 6

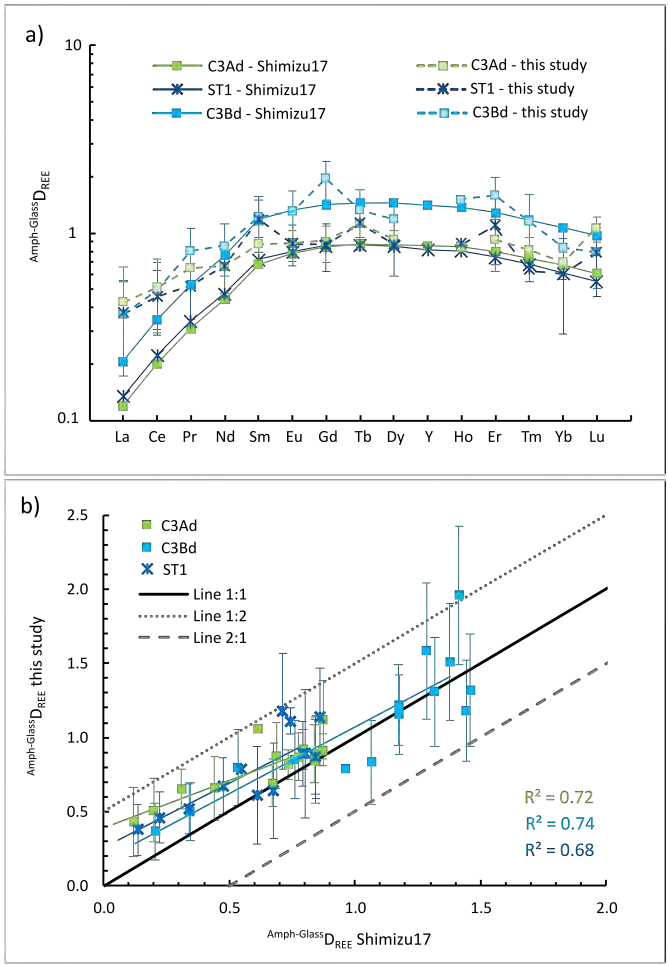
a)
10
1
0.1
Amph-Glass DREE
C3Ad - Shimizu17
ST1 - Shimizu17
C3Bd - Shimizu17
C3Ad - this study
ST1 - this study
C3Bd - this study
La Ce Pr Nd Sm Eu Gd Tb Dy Y Ho Er Tm Yb Lu
b)
2.5
2.0
1.5
1.0
0.5
0.0
Amph-Glass DREE this study
C3Ad
C3Bd
ST1
Line 1:1
Line 1:2
Line 2:1
R² = 0.72
R² = 0.74
R² = 0.68
0.0 0.5 1.0 1.5 2.0
Amph-Glass DREE Shimizu17

$$\ln D_{Th} = 8.985 * X_{Th}/X + 4.141 * Mg\#_{Amph} - 8.285$$

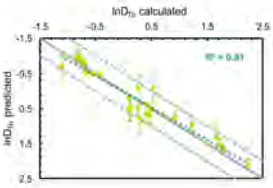

Regression Statistics	
Multiple R	0.96
R Square	0.91
Adjusted R Square	0.91
Standard Error	0.28
Observations	27

ANOVA

	df	*SS*	*Significance F*
Regression	2	19.60	1.82E-13
Residual	24	1.86	
Total	26	21.46	

	Coefficients	*Standard Error*	*t Stat*	*P-value*
Intercept	-8.28	0.77	-10.72	1.23E-10
X Variable 1	8.99	0.60	15.01	1.06E-13
X Variable 2	4.14	0.65	6.41	1.24E-06

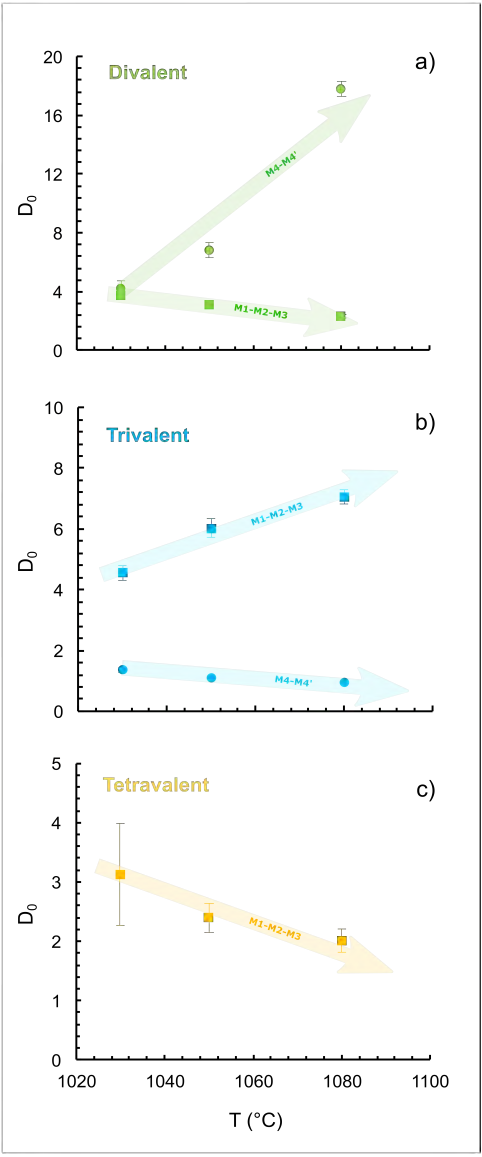
a)
Divalent
M4-M4'
M1-M2-M3
D0
b)
Trivalent
M1-M2-M3
M4-M4'
D0
c)
Tetravalent
M1-M2-M3
D0
T (°C)

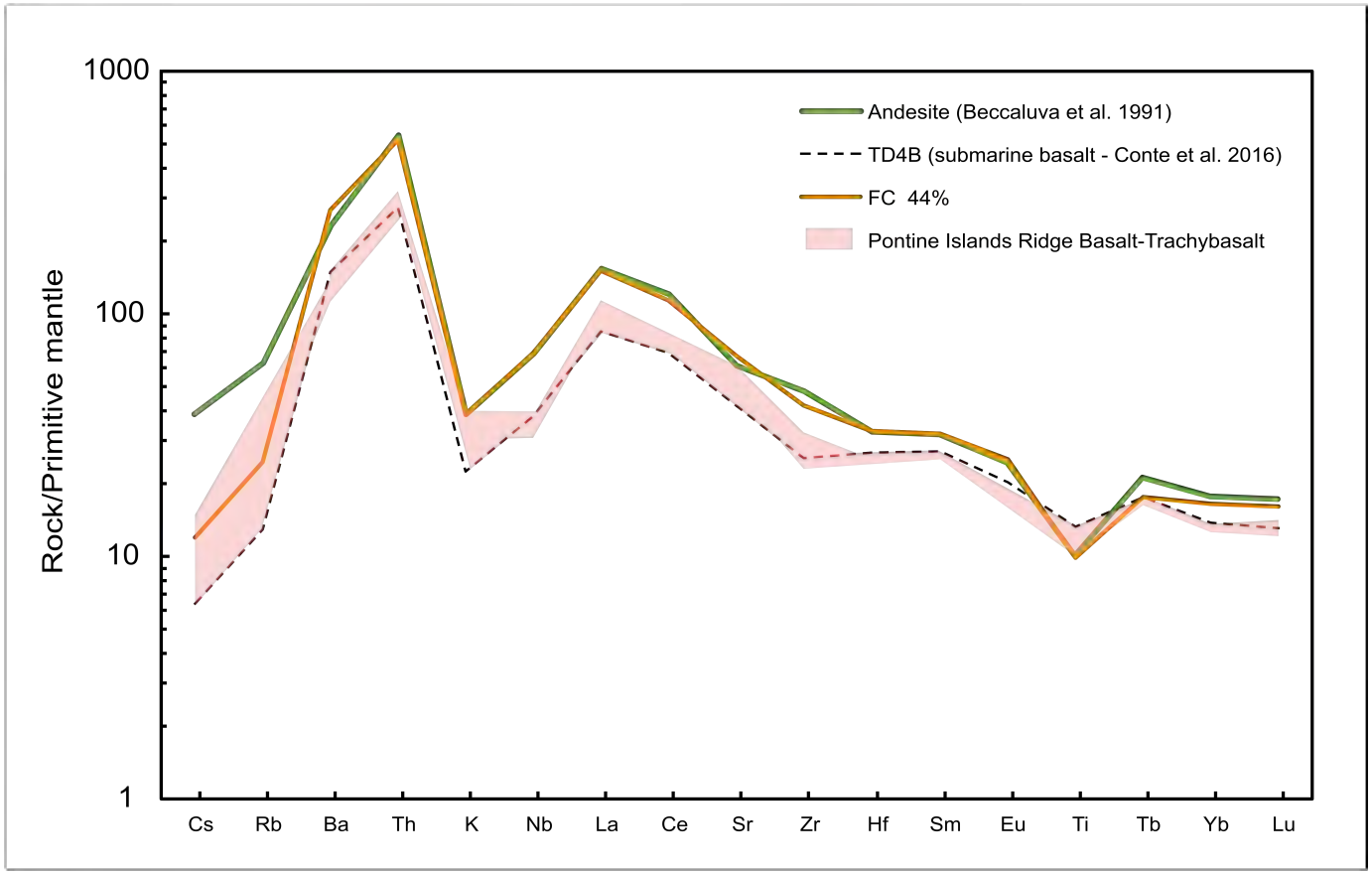
1000
100
10
1
Rock/Primitive mantle
Andesite (Beccaluva et al. 1991)
TD4B (submarine basalt - Conte et al. 2016)
FC 44%
Pontine Islands Ridge Basalt-Trachybasalt
Cs
Rb
Ba
Th
K
Nb
La
Ce
Sr
Zr
Hf
Sm
Eu
Ti
Tb
Yb
Lu

Table 1 Composition (wt%) of APR16 rock sample and APR16GL starting material

Sample	APR16	APR16GL
SiO_2	48.89	49.3 (0.46)
TiO_2	1.23	1.33 (0.03)
Al_2O_3	15.65	15.31 (0.14)
FeO_{tot}	8.08	7.79 (0.13)
MnO	0.14	0.14 (0.05)
MgO	8.89	9.31 (0.07)
CaO	11.64	12.02 (0.09)
Na_2O	2.88	2.86 (0.05)
K_2O	1.52	1.60 (0.02)
P_2O_5	0.31	0.55 (0.02)
Total	99.23	99.31 (0.29)[¥]
L.O.I.	0.61	-
Mg# *	0.66	0.68

*[MgO/(MgO+FeO_{tot})] molar, assuming all Fe^{2+} and Fe^{3+} as FeO_{tot}. Chemical composition of APR16 is from D'Antonio et al. (1999); APR16GL composition is from Perinelli et al. (2019). [¥] For APR16GL the analysis is normalized to 100 but the original total is reported. Standard deviation is reported in parenthesis.

Table 2 Experimental run conditions, melt water contents, phases assemblage and proportions in run products

Run #	T (°C)	T_L (°C)	ΔT (°C)	Time (h)	H_2O_i (wt%)	Phases	H_2O_f EPMA (wt%)	Σr^2	% $\Delta Fe^{\S}$
APR16-C3Aa*	1080	1218	138	0.25	4	Gl + Amph + Cpx + Plg + Ox			
APR16-C3Ab*	1080	1218	138	3	4	Gl + Amph + Cpx + Plg + Ox	7.5		
APR16-C3Ad	1080	1233	153	9	3.3	Gl(55) + Amph(24) + Cpx(20) + Ox(1)	10.2	0.41	-1
APR16-C3Ba*	1030	1224	194	0.25	3.8	Gl + Amph + Cpx + Plg + Ox	10.6		
APR16-C3Bb*	1030	1225	195	3	3.7	Gl + Amph + Cpx + Plg + Ox	9.5		
APR16-C3Bc*	1030	1232	202	6	3.4	Gl + Amph + Cpx + Opx + Ox			
APR16-C3Bd	1030	1216	186	9	4.2	Gl(40) + Amph(35) + Cpx(24) + Ox(1)	8.3	0.18	-1
APR16-ST1	1050	1150	100	2	8	Gl(51) + Amph(36) + Cpx(13) + Ox(1)	8.1	0.31	

Gl = glass; Amph = amphibole; Cpx = clinopyroxene; Opx = orthopyroxene; Plg = plagioclase; Ox = oxide minerals. ΔT is the difference between the liquidus temperature and the nominal temperature of the experiment. T_L is the liquidus temperature (°C) determined on the basis of phase relations experimental data from Perinelli et al. (2019). H_2O_f EPMA = water content in the melt determined by the by-difference calculation method (respect to the total of EMP analyses); % Percent of relative Fe loss from starting material based on difference between the starting material and calculated bulk composition of experiment obtained from mass-balance calculations. Σr^2 values from mass balance calculation. *Crystals too small for analysis and not considered for mass balance calculations.

Table 3 Major and trace element concentrations (ppm) for synthetic amphibole crystals and glasses

Run#	APR16-C3Aa	APR16-C3Ab	APR16-C3Ad	APR16-C3Ba	APR16-C3Bb	APR16-C3Bc	APR16-C3Bd	APR16-ST1
Phase	Amph glass	Amph glass	Amph glass	Amph glass	Amph glass	Amph glass	Amph glass	Amph glass
Na*	18472 (838)	16766 (307)	16469 (351) 21514 (213)	14763 (265)	13353 (302)	10831 (452)	17211 (513) 17730 (231)	16840 (433) 20698 (211)
K*	11456 (102)	11124 (52)	11207 (103) 16769 (206)	11207 (98)	13448 (92)	10709 (232)	8965 (272) 21168 (209)	9630 (312) 15025 (204)
Ca*	80121 (5800)	82051 (6100)	83337 (5980) 56892 (3850)	84409 (4800)	86196 (6400)	88912 (5100)	84909 (5150) 43026 (3105)	90556 (4350) 59608 (3400)
Fe*	82005 (4451)	65526 (2350)	59774 (2310) 46327 (950)	71123 (1890)	66537 (1930)	76952 (2100)	70812 (2250) 29382 (890)	68635 (1850) 42285 (850)
Mg	51270 (4251)	55950 (3402)	71267 (16478) 25466 (2086)	57857 (3171)	56380 (1819)	79820 (18651)	56740 (13767) 19200 (3389)	77962 (14804) 26575 (4189)
Al	83550 (13055)	75983 (5265)	79183 (11744) 100157 (5379)	87900 (2712)	89100 (1880)	100340 (5010)	79311 (15056) 103500 (35003)	79892 (10591) 109100 (18949)
Mn	1269 (112)	1199 (79)	1048 (173) 1283 (46)	1373 (93)	1355 (23)	1557 (142)	1153 (197) 995 (135)	1048 (139) 1381 (207)
Ti	6426 (788)	7453 (904)	8157 (2071) 5949 (324)	7266 (195)	7280 (86)	8838 (2971)	7906 (2131) 3633 (239)	7787 (1151) 5452 (509)
Zr	107 (19)	90 (4)	69 (26) 149 (15)	105 (3)	106 (1)	101 (9)	75 (24) 163 (40)	77 (16) 154 (24)
Nb	12 (2)	10.1 (0.6)	7.4 (3.3) 17.6 (1.4)	12 (1)	11.9 (0.4)	13 (2)	8 (2) 20 (5)	8 (2) 19 (4)
Hf	2.9 (0.6)	2.1 (0.3)	2.3 (0.9) 3.2 (0.3)	2.7 (0.4)	2.7 (0.6)	3.3 (0.4)	2.4 (0.8) 3.04 (0.01)	2.7 (0.5) 3.6 (0.9)
Ta	0.71 (0.14)	0.7 (0.1)	0.66 (0.11) 0.99 (0.05)	0.7 (0.1)	0.7 (0.1)	0.6 (0.1)	0.6 (0.2) 1.2 (0.1)	0.7 (0.1) 1.2 (0.3)
Th	3.32 (0.86)	2.1 (0.3)	2.31 (0.94) 4.7 (0.4)	3.0 (0.2)	2.8 (0.1)	2.7 (0.5)	1.9 (0.9) 5.8 (0.3)	1.7 (0.8) 5.9 (1.6)
U	1.06 (0.28)	0.82 (0.08)	0.75 (0.05) 1.5 (0.1)	1.0 (0.1)	0.9 (0.1)	0.9 (0.1)	0.7 (0.3) 1.9 (0.4)	0.7 (0.2) 1.8 (0.4)

Rb	61 (16)	40 (3)	34 (18) 86 (7)	62 (11)	61 (3)	38 (7)	39 (17) 103 (20)	35 (14) 87 (18)
Sr	518 (107)	435 (32)	429 (91) 679 (24)	484 (96)	539 (15)	555 (43)	422 (88) 708 (103)	407 (80) 733 (136)
Cs	2.7 (0.8)	1.6 (0.4)	1.8 (0.1) 4.1 (0.5)	2.7 (0.4)	2.3 (0.1)	2.2 (0.1)	2.0 (0.7) 5 (1)	1.7 (0.5) 4 (1)
Ba	507 (125)	414 (37)	377 (104) 729 (56)	491 (100)	523 (11)	450 (61)	376 (111) 791 (139)	354 (93) 761 (164)
Pb	9 (5)	1.4 (0.7)	bdl 0.51 (0.07)	17 (9)	31 (23)	1.44 (*0.36*)	0.83 (0.18) bdl	0.85 (0.13) 1.17 (0.03)
Sc	40 (5)	42 (3)	50 (10) 18 (2)	43 (3)	43 (1)	50 (5)	41 (7) 16 (3)	60 (9) 19 (3)
V	189 (18)	208 (23)	163 (26) 223 (3)	209 (12)	210 (2)	264 (61)	198 (39) 146 (18)	154 (30) 212 (31)
Cr	337 (41)	355 (30)	525 (173) bdl	377 (15)	375 (7)	436 (68)	381 (96) 175 (9)	612 (208) 200 (28)
Co	36 (8)	38 (3)	44 (8) 23 (2)	45 (4)	46 (2)	52 (18)	42 (12) 13 (2)	49 (10) 22 (3)
Ni	119 (37)	135 (16)	184 (70) 13 (4)	148 (22)	165 (16)	167 (66)	149 (52) 37 (5)	241 (75) 40 (17)
La	16.7 (3.3)	13.3 (0.7)	11 (5) 25 (1)	17 (1)	17 (1)	16 (1)	11 (5) 30 (8)	10 (4) 26 (5)
Ce	34 (4)	30 (1)	25 (10) 48 (1)	35 (1)	35 (1)	37 (4)	25 (9) 50 (7)	23 (7) 50 (10)
Pr	4.2 (0.8)	3.8 (0.3)	3.8 (0.8) 48 (1)	4.4 (0.3)	4.6 (0.1)	4.6 (0.4)	4 (1) 5 (1)	3 (1) 6 (1)
Nd	18.4 (2.9)	18.5 (1.3)	16.2 (5.2) 25 (1)	21 (2)	19.8 (1.7)	23.7 (2.9)	17 (4) 20 (4)	16 (3) 24 (5)
Sm	4.4 (0.5)	4.8 (0.5)	4.5 (1.0) 5.2 (0.5)	5 (1)	5.1 (0.7)	5.5 (1.5)	5 (1) 4.1 (0.4)	5 (1) 4 (1)
Eu	1.6 (0.3)	1.6 (0.3)	1.5 (0.2) 1.7 (0.4)	1.8 (0.4)	1.8 (0.3)	2.0 (0.4)	1.7 (0.4) 1.3 (0.2)	1.6 (0.3) 1.8 (0.3)
Gd	4.9 (0.9)	4.8 (0.5)	4.4 (0.9) 4.9 (0.4)	4.6 (0.8)	4.9 (0.4)	5.4 (1.6)	4.7 (1.1) 3.7 (0.1)	5.2 (1.2) 6 (1)

Tb	0.7 (0.1)	0.7 (0.1)	0.8 (0.2)	0.8 (0.1)	0.7 (0.1)	0.8 (0.2)	0.7 (0.2)	0.8 (0.2)
			0.74 (0.04)				0.53 (0.01)	0.7 (0.1)
Dy	3.8 (0.5)	3.9 (0.9)	3.6 (0.2)	4.2 (0.6)	4.1 (0.5)	5.0 (0.8)	3.8 (1.1)	4 (1)
			3.9 (0.4)				3.22 (0.01)	4.6 (0.9)
Ho	0.8 (0.1)	0.8 (0.2)	0.7 (0.1)	0.8 (0.1)	0.9 (0.1)	1.0 (0.1)	0.8 (0.2)	0.8 (0.1)
			0.85 (0.05)				0.53 (0.06)	0.9 (0.1)
Er	2.2 (0.5)	1.93 (0.32)	2.02 (0.62)	2.3 (0.2)	2.4 (0.2)	2.4 (0.8)	2.1 (0.5)	2.0 (0.4)
			2.2 (0.2)				1.32 (0.13)	1.8 (0.6)
Tm	0.27 (0.05)	0.34 (0.03)	0.27 (0.03)	0.35 (0.01)	0.4 (0.1)	0.37 (0.13)	0.3 (0.1)	0.32 (0.04)
			0.33 (0.04)				0.26 (0.04)	0.50 (0.03)
Yb	1.88 (0.32)	2.1 (0.3)	1.6 (0.1)	1.96 (0.04)	2.5 (0.5)	2.11 (0.27)	1.83 (0.43)	1.97 (0.47)
			2.3 (0.3)				2.2 (*0.5*)	3.2 (*0.7*)
Lu	0.35 (0.08)	0.4 (0.1)	0.37 (0.02)	0.34 (0.03)	0.3 (0.1)	0.29 (0.06)	0.3 (0.1)	0.34 (0.12)
			0.35 (0.05)				0.38 (0.05)	0.43 (*0.08*)

Notes: Amph = amphibole; standard deviation is reported in brackets. *Data from EPMA.
For single analysis Int2SE (i.e., analytical error) is reported also in brackets but in italic; bdl = below detection limit.

Table 4 Major and trace elements partition coefficients between amphibole and glass for experimental samples

Run#	APR16-C3Ad	APR16-C3Bd	APR16-ST1
Na*	0.77 (0.02)	0.97 (0.03)	0.81 (0.02)
K*	0.67 (0.01)	0.42 (0.01)	0.64 (0.02)
Ca*	1.46 (0.12)	1.97 (0.16)	1.52 (0.10)
Fe*	1.29 (0.05)	2.41 (0.12)	1.62 (0.05)
Mg	2.79 (0.69)	2.95 (0.88)	2.93 (0.77)
Al	0.79 (0.12)	0.76 (0.29)	0.73 (0.17)
Al^{IV}	0.64	0.60	0.61
Al^{VI}	0.14	0.15	0.12
Mn	0.82 (0.14)	1.16 (0.25)	0.79 (0.16)
Li	0.84 (0.20)	0.75 (0.21)	0.37 (0.08)
Ti	1.37 (0.36)	2.16 (0.60)	1.43 (0.25)
Zr	0.46 (0.18)	0.46 (0.19)	0.50 (0.13)
Nb	0.42 (0.14)	0.45 (0.15)	0.42 (0.15)
Hf	0.71 (0.28)	0.78 (0.25)	0.77 (0.24)
Ta	0.67 (0.12)	0.48 (0.17)	0.61 (0.20)
Th	0.49 (0.20)	0.34 (0.16)	0.29 (0.16)
U	0.50 (0.05)	0.37 (0.16)	0.39 (0.13)
Cs	0.44 (0.27)	0.40 (0.16)	0.43 (0.16)
Rb	0.40 (0.21)	0.38 (0.18)	0.40 (0.18)
Sr	0.63 (0.14)	0.60 (0.15)	0.56 (0.15)
Ba	0.52 (0.15)	0.48 (0.16)	0.47 (0.16)
Pb			0.73 (0.11)
Sc	2.73 (0.62)	2.56 (0.65)	3.16 (0.69)
V	0.73 (0.12)	1.36 (0.32)	0.73 (0.18)
Cr		2.18 (0.56)	3.06 (1.12)
Co	1.93 (0.38)	3.23 (1.05)	2.23 (0.55)
Ni	9.42 (4.15)	4.03 (1.51)	6.03 (3.17)
La	0.43 (0.23)	0.37 (0.19)	0.38 (017)
Ce	0.51 (0.22)	0.50 (0.19)	0.46 (0.17)
Pr	0.66 (0.13)	0.80 (0.26)	0.52 (0.17)
Nd	0.66 (0.21)	0.85 (0.26)	0.67 (0.19)
Sm	0.88 (0.22)	1.22 (0.27)	1.18 (0.39)
Eu	0.87 (0.16)	1.31 (0.37)	0.89 (0.22)
Gd	0.89 (0.20)	1.27 (0.47)	0.87 (0.25)
Tb	1.12 (0.26)	1.32 (0.38)	1.14 (0.33)
Dy	0.92 (0.11)	1.18 (0.34)	0.87 (0.28)
Ho	0.85 (0.10)	1.51 (0.41)	0.89 (0.15)
Er	0.92 (0.29)	1.58 (0.40)	1.11 (0.43)
Tm	0.82 (0.13)	1.15 (0.46)	0.64 (0.09)
Yb	0.69 (0.10)	0.84 (0.27)	0.61 (0.19)
Lu	1.06 (0.16)	0.79 (0.28)	0.79 (0.32)

Table 5 Best fits for E, r_0 and D_0 obtained by regression of amphibole/liquid partition coefficients of monovalent, divalent, trivalent and tetravalent cations in A, M1-M2-M3, M4-M4' sites

		APR16-C3Ad	APR16-ST1	APR16-C3Bd
Monovalent	**A**			
	D_0	0.97±0.20	0.86±0.06	0.98±0.11
	r_0	1.449±0.049	1.495±0.008	1.419±0.030
	E	*30±4*	30±4	*30±4*
Divalent	**M1, M2, M3**			
	D_0	2.32±0.14	3.11±0.09	3.77±0.30
	r_0	0.689±0.006	0.686±0.008	0.697±0.013
	E	209±5	200±1	247±37
	M4, M4'			
	D_0	17.77±0.51	6.84±0.53	4.24±0.47
	r_0	0.709±0.002	0.776±0.008	0.834±0.015
	E	202±2	227±20	259±48
Trivalent	**M1, M2, M3**			
	D_0	7.08±0.09	6.04±0.28	4.56±0.25
	r_0	0.689±0.004	0.688±0.002	0.688±0.004
	E	785±12	805±10	696±27
	M4, M4'			
	D_0	0.9550±0.0002	1.1004±0.0018	1.3541±0.0634
	r_0	1.0514±0.0001	1.0558±0.0007	1.0511±0.0006
	E	200±1	299±4	303±17
Tetravalent	**M1, M2, M3**			
	D_0	2.004±0.194	2.39±0.24	3.12±0.86
	r_0	0.6475±0.0038	0.6477±0.0034	0.6368±0.0117
	E	1195±143	1247±137	1181±429

Note: D_0: strain-compensated partition coefficient. E: Young Modulus of the lattice site (GPa). r_0: optimum site radius (Å). D_0, r_0 and E were calculated using the SIMPLE program (Dalou et al. 2018). E values of the monovalent cations (reported in italic) for APR16-C3Ad and APR16-C3Bd runs have been set equal to that determined for run APR16-ST1.